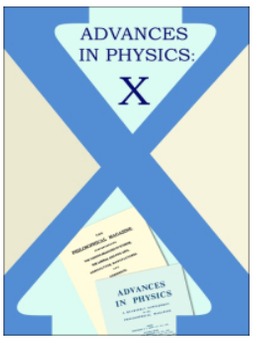

Advances in Physics: X

ISSN: (Print) (Online) Journal homepage: https://www.tandfonline.com/loi/tapx20

# Future applications of the high-flux thermal neutron spectroscopy: the ever-green case of collective excitations in liquid metals

Caterina Petrillo & Francesco Sacchetti

**To cite this article:** Caterina Petrillo & Francesco Sacchetti (2021) Future applications of the high-flux thermal neutron spectroscopy: the ever-green case of collective excitations in liquid metals, Advances in Physics: X, 6:1, 1871862, DOI: 10.1080/23746149.2021.1871862

**To link to this article:** https://doi.org/10.1080/23746149.2021.1871862



Published online: 07 Feb 2021.

ADVANCES IN PHYSICS: X
2021, VOL. 6, NO. 1, 1871862
https://doi.org/10.1080/23746149.2021.1871862

Taylor & Francis
Taylor & Francis Group

REVIEW



# Future applications of the high-flux thermal neutron spectroscopy: the ever-green case of collective excitations in liquid metals

Caterina Petrillo[a] and Francesco Sacchetti[a,b]

[a]Department of Physics & Earth Science, University of Perugia, Perugia, Italy; [b]National Research Council, Institute IOM-CNR, Perugia, Italy

**ABSTRACT**

The European landscape of neutron sources for research applications is changing and the major European joint effort, the European Spallation Source (ESS) currently under construction in Lund (Sweden), is progressing. The high flux source ESS is designed to deliver slow neutrons with a long-pulse time structure, a rather unique feature, with characteristics optimised to maximise the instrument performances and the experimental throughput. This is expected to result in unprecedented scientific capability over broad research areas. Major breakthroughs are likely to take place in the understanding of complex, strongly interacting and disordered systems, more specifically on their dynamical response. This will have an impact on the development of novel theories to cover some of the presently existing knowledge gaps and will prompt advanced applications of the investigated materials. Liquid metals are a prototypical example of complex systems extensively studied from the sixties on, now re-emerging as powerful functional materials for unconventional and broad spectrum applications. Research on liquid metal composites will benefit of the new experimental possibilities available at the ESS. We review the status of the experiments on liquid metals dynamics, focusing on a selected set of systems, and discuss the perspectives for cutting-edge experiments at the new sources.

**ARTICLE HISTORY**
Received 17 November 2020
Accepted 23 December 2020

**KEYWORDS**
Neutron scattering; new sources; liquid metals; collective excitations; THz dynamics

**CONTACT** Caterina Petrillo caterina.petrillo@unipg.it Department of Physics & Earth Science, University of Perugia, Perugia I-06123, Italy.

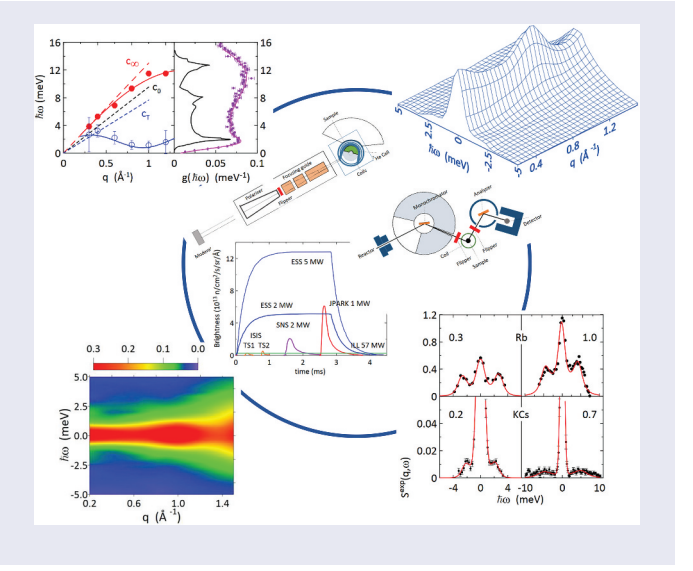


## 1. Introduction

Scattering of slow neutrons is a well-established technique, nowadays routinely applied to the investigation of atomic-scale structural, magnetic and dynamical properties of materials [1–4]. Complementing the neutron technique with the companion photon or electron scattering methods represents a notable example of how a multi-messenger approach can work in condensed matter research [5–9]. Indeed, tackling a specific problem by different and highly complementary techniques can provide for a complete description and a deeper understanding of the material properties. If, in 1949, Alvin Weinberg, Research Director at Oak Ridge (US), could state that neutron diffraction *has become an extraordinarily powerful tool for the investigation of the structure of hydrogen-containing crystals* [10], so anticipating the impact of the technique on the study of biological samples with the modern deuteration benefits, and in 1951 the first magnetic neutron diffraction measurements on transition metal oxides by the Nobel laureate Clifford Shull [11], which provided experimental evidence of the antiferromagnetic ordering, were received as a surprise by the scientific community [12], along the years the production and exploitation of neutron beams as a clean, non-destructive and unique characterisation tool has become part of routine research work.

The interaction of thermal neutrons with matter is governed by the intrinsic properties of this probe, namely the absence of charge and the existence of a magnetic moment, a de Broglie wavelength comparable with the interatomic distances in solids and the bond lengths in liquids, and an associated energy of the same order as the elementary excitations in solids,

which make possible to measure interference effects in diffraction patterns and to map energy spectra and dispersion of vibrational and magnetic modes. Electrical neutrality brings about deep penetration into materials and makes neutron the election probe of bulk properties. The nature of the nuclear interaction also makes neutrons equally sensitive to heavy and light atoms, and favours its application to probe hydrogen-containing samples, while the different coupling to the isotopes of a same element makes the technique of the isotopic substitution a valuable tool to increase the information on a given chemical sample.

When compared to photon sources, a major limitation of the neutron technique is the effective thermal neutron flux, which is very slowly rising with the years as a consequence of the achieved maturity in the source (nuclear reactor or spallation-based accelerators) design and performance. The way to overcome such an intrinsic limitation has been a large investment into the upgrade of the instrumentation [13,14], pushing for innovative solutions for targets and moderators [15,16], neutron optical systems (monochromators, guides, mirrors, collimators, choppers, …), detector technologies and data acquisition and analysis. This approach has contributed to improve the performances of the instruments optimising the fluxes effectively available at the sample and actually detected after the scattering process, so increasing the reach of the scientific experiments.

A key advance in the present landscape of neutron facilities [17] is expected to result from the operation of the future source ESS [18] where the main design parameters, namely the time structure of the source [19], the moderator design [20] and the characteristics of the instrument suite

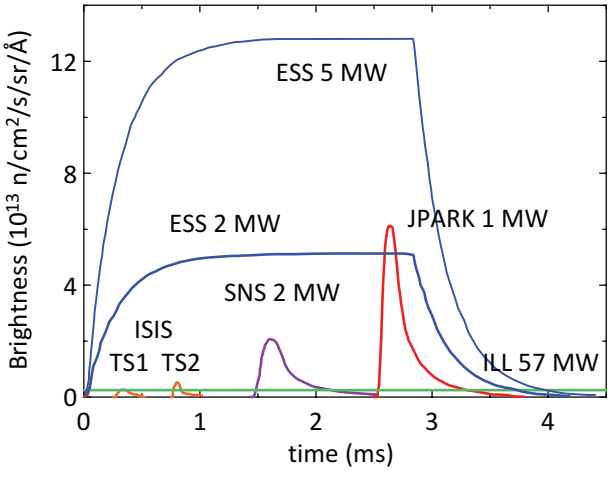


**Figure 1.** Time-dependent brightness at a wavelength $\lambda = 5$ Å for the major spallation neutron sources ISIS (UK), SNS (US), J-PARC (Japan) and the continuous reactor source of the ILL (FR), in comparison with the performances expected with the cold moderator at the ESS operated at 2 MW and 5 MW.

[21], were optimised to obtain a high spectral brightness for as many beamports as possible while favouring the performances for cold-neutron applications. The ESS expected performances are shown in Figure 1 in comparison with the major operating neutron facilities: the higher brightness of the ESS for cold neutrons (plot at $\lambda$ = 5 Å) spanning over 2.86 ms pulse length is apparent.

While the scientific case for a broad range of applications enabled by operating ESS has been widely presented, here we want to point out at some specific characteristics of the future facility that, if successfully exploited, would make significant developments possible in the research field of complex, disordered systems like liquids.

A very special feature of neutron scattering from nuclei is the presence of the so-called incoherent contribution to the cross-section, which adds to the coherent term [1,2]. The incoherent contribution originates from the intrinsic nature of the nuclear interaction and substantially accounts for the isotopic distribution inside the sample and the coupling of the nuclear spin with the neutron spin, that is the scattering length varies to one nucleus to another of the sample. This feature has been always perceived as a limitation of the technique because, despite the value of simultaneously probing the collective (coherent) and single-particle (incoherent) dynamics of a system, decoupling the two contributions in the measured cross-section is not straightforward. This property, however, could turn round into an advantage at the high brilliance sources where the high flux available could make the polarisation analysis technique [1,2,22–26], by which the incoherent contribution to the cross-section can be sorted out, a rather standard tool for applications outside the more typical field of magnetism [2,27–30]. Indeed, despite polarisation analysis is a well-known approach to obtain the full information carried by the neutron cross-section, as demonstrated by the pioneering experiment of [25], it was mostly applied to the study of magnetic elastic processes of crystal diffraction [31–33], while broadening the scientific scope to quasi-elastic neutron scattering in disordered and fluid samples occurred in rather recent years [34–38]. Adding the polarisation analysis option to the incoming and diffused neutron beams in inelastic scattering experiments designed to measure the system dynamics, typically produces such a poor counting statistics to discourage its use as a means to extract the incoherent contribution. This condition, however, could change at a high-intensity source like the ESS, making polarisation option an advanced technological standard for inelastic experiments. Being able to separately measure the incoherent and the coherent contributions to the scattering would boost full exploitation of the complementarity with the x-ray scattering techniques where the purely coherent dynamical response of the system is probed.

A further opportunity at the new intense sources is represented by the possibility of measuring the response function of the system with higher statistics at exchanged wavevectors $q$ and energies $\hbar\omega$ close to the boundaries of the kinematic region allowed by the scattering process, or in the limiting regions of very low $q$ and/or high $\hbar\omega$ values. Indeed, the kinematic region accessible to the neutron scattering experiment is defined by the momentum and energy conservation laws, and the possibility to measure a collective excitation, with a given dispersion relation, depends on the ratio between the mode and the probe velocities. This constraint, of course, cannot be lifted, as it derives from the neutron having a finite mass. However, increasing the intensity at the sample allows for a higher statistics and a better discrimination of the signal from the background especially in the low $q$ region, thus improving the *visibility* of the excitation mode.

Exploiting the ESS brightness coupled to the optimised design of high-intensity inelastic spectrometers with polarisation analysis option [21], would enable to obtain the full wavevector and energy-dependent response function with the simultaneous separate measurement of single-particle dynamics and collective excitations in liquids, thus complementing the x-ray experiments at the synchrotron radiation sources and providing solid experimental support to the theories of the liquid state. Moreover, a combined neutron and x-ray investigation of the collective modes in liquids would benefit of both the typical neutron Gaussian-shaped energy and wavevector resolution function, and the wide dynamic range accessible to the inelastic x-ray instruments characterised by a broad-tail energy resolution function. Indeed, low energy excitations can be better distinguished by the neutron probe because of the short-tailed Gaussian resolution in a region where the kinematic restrictions are less critical, with the x-rays that do not suffer kinematic restrictions and provide accurate measurements of the modes at higher energy where the longer tails of the resolution do not affect the experimental data.

Here we report on inelastic neutron scattering experiments tailored to measure the collective, coherent dynamics in liquid metals, and show the added value of measuring the inelastic incoherent response to obtain a fully consistent picture of the system. The role of the collective excitations for a theoretical description of the liquid state, and specifically the liquid metals, is discussed (Section 2.) and the experimental approach and technique analysed (Sections 3. and 4.). A summary of the existing data and interpretation mostly in liquid alkali metals is presented outlining the major conclusions on the microscopic dynamics of the selected systems and pointing out at the still open issues (Section 5.). A general theoretical approach to model the dynamic response in disordered systems, based on the picture of interacting modes, is reported (Section 6.) and applied to the analysis of the two paradigmatic cases of liquid mercury and liquid gallium

(Section 7.). The new analysis contributes to clarify observed features of the spectra which still lack of consistent interpretation. Much support to correctly frame the response of these systems comes from the analysis of the unpublished incoherent cross-section data in mercury which are here discussed jointly with the interacting mode model. The case of lithium-ammonia solutions, a rare example of low-density electron system, is analysed using new data to obtain concentration-dependent data of the THz velocity. Finally, we briefly discuss the perspectives for these studies offered by the new high-flux sources coming on-line with an outlook on future developments and investigations in complex disordered systems, like biomaterials in Section 8.

## 2. The importance of collective excitations in liquids. The case of liquid metals

The liquid state itself is complicated [39] and a general, unified theory of liquids is actually not developed, despite continuous progress in modelling the liquid properties in well-defined, although restricted, thermodynamic conditions [40–46]. Known difficulties when dealing with liquids derive from the combined existence of strong inter-atomic interactions and large atomic displacements, which reduces the effectiveness of the theoretical standard tools applied to describe the limiting regimes of low-density gases and crystalline solids. With high-performance computing getting available, large-scale molecular dynamics (MD) simulations became a common and effective approach to describe the liquid state at atomic level [47]. Although MD classical calculations bring in much more information than experimentally measurable, like atomic trajectories, the computational approach sometimes lacks the physical insight enabling a formal description of the liquid state. Interest in understanding and modelling the properties that a system shows when in liquid phase remains proven by the huge literature, either theoretical or experimental, on the subject [48–57]. A series of recent theoretical papers efficaciously delineate the difficulties of a general theory of the liquid state and propose an operational approach based on the recognition of a liquid as a system in a *mixed* dynamical state [58–62] combining features of the solid and the gas microscopic dynamics. The scheme there recommended bypasses long-standing debates on the liquid description being obtained by extrapolating theories developed for gases or, at the other extreme, for solids.

A peculiar behaviour observed experimentally in most liquids, which ignited the debate on the theoretical approach best suited to describe the liquid state and its dynamics, is the existence of high-frequency collective modes, that is coherent propagating oscillations, extending well beyond the long-wavelength limit and characterized by a non-linear dispersion up to

wavevectors of the order of $q_0/2$, $q_0$ the first peak position of the static structure factor [63–76]. Features of these high-frequency coherent excitations, like the so-called *positive* dispersion of the longitudinal mode with associated propagation velocity higher than the ordinary sound in the liquid, and the emergence of transverse-character oscillations [77–82] resembling phonon modes in solids, are not predicted by classical hydrodynamics. The introduction of a properly defined *relaxation time* $\tau$ enables distinguishing between the two regimes of the liquid dynamics, namely the hydrodynamic regime characterized by $\omega\tau \ll 1$ where the hydrodynamics equations provide an appropriate description of the long wavelength behaviour, and the solid-like regime entering for $\omega\tau \gg 1$ where the longitudinal mode continues to propagate and the existence of propagating transverse modes is possible. However, despite the huge development of theoretical schemes, of new models and extensive simulation work, still many are the open issues and unanswered questions towards the understanding of the liquid collective dynamics over the kinematic region centred at $q\sim$ 1 Å$^{-1}$ and $\hbar\omega\sim$ 25 meV. It is over this region that neutron and x-ray inelastic scattering experiments are optimally suited to probe the coherent collective excitations and, in the case of neutrons, also the single-particle incoherent response.

Historically, liquid metals were among the first fluid systems whose microscopic dynamics was investigated by neutron scattering [83] as early as the first three-axes neutron spectrometer became available in 1950s [84]. References to the first neutron experiments are found in [51]. A landmark experiment is certainly that on liquid Rubidium carried out by Copley and Rowe in 1974 [63] which, for the first time, showed unambiguously the existence of a long-living collective mode, and was accompanied by the notable work of Rahman who, in the same year, published the molecular dynamics simulation [85] of the microscopic dynamics in Rubidium. Extensive studies of liquid metals followed, with inelastic neutron scattering being the qualifying technique until mid-nineties [2]. A major and renewed drive to the study of collective excitations came from the operation of new generation synchrotron radiation sources that made possible high-resolution inelastic x-ray scattering experiments, notably on liquid metals [65]. A review of the extensive work carried out by x-ray scattering to measure collective excitations in liquid metals is given in [52]. A rather large body of information is now available from the experiments probing the dynamic response at THz frequency and microscopic wavevector range in a variety of liquid metals, from alkali metals and their alloys to polyvalent and transition metals, over a wide range of thermodynamic states.

In comparison with other more common liquid systems, like molecular and organic liquids, molten metals are simpler benchmarks for testing the models of liquid dynamics, while representing an ideal playground to address the fundamental topic of the dynamic screening phenomena in the interacting electron gas [86]. The measured coherent response function of liquid metals contains a longitudinal acoustic mode characterized by a rather well-defined dispersion over an extended range of exchanged wavevectors, even though, and very interestingly, recent studies show a more complex dynamics with the presence of a second low-energy mode that has been identified as a transverse acoustic-like excitation [78–82]. Also, interpretation schemes accounting for the screened Coulomb interaction among the ions [87] and its effect on the collective excitations, enabled identifying common trends in the experimental data for alkali metals [53,64,88], alkali earths and polyvalent metals [89]. We remark that, beyond the focus on the propagating ion density fluctuations, molten alkali metals are considered the prototype of a liquid *simple* metal [87,90], that is a system characterised by an almost-free electron band structure in the crystalline state, which, together with the homogeneity approximation, represents an invaluable test bed for the interacting electron gas theory and the dynamic screening response in the electron plasma activated by the ionic charge disturbance [91]. Under this perspective, the liquid phase of simple metals provides experimentally feasible and easy conditions for testing the electron plasma phenomena. However, gaps remain in the knowledge of the microscopic mechanisms responsible for the propagation of collective excitations in liquid metals, despite their *simplicity*, and a consistent theoretical interpretation is not well defined yet.

The reasons for studying molten and liquid metals go beyond those of fundamental physics and today they are emerging as key materials for technological applications with a large potential for a broad use, ranging from electronics to medicine. Indeed, these systems couple the generally good electrical and thermal conductivities of the metal with mechanical flexibility, elasticity and low viscosity and, in some cases, with a high biocompatibility. The presence of highly mobile conduction electrons is an intrinsic characteristics of metals which is maintained at melting, making the electrical conductivities of molten simple liquid metals, like alkali metals, very close to the typical values of the solid state, i.e. $10 - 40\mu\Omega \cdot \mathrm{cm}$ in resistivity [92]. These values also explain the high thermal conductivities of liquid metals. Very recent reviews on liquid metals and composites with an overview on their perspective applications are found in [93–96]. Of major technological interest are the metals that are found in liquid phase around room temperature (RT), notably Hg, Cs, Fr, Ga, and a series of alloys characterized by an eutectic point around RT [92] among

which the recently proposed Ga-based eutectic alloys (Ga-In, Ga-Sn, Ga-In-Sn) [95,96].

Here, as anticipated, we focus on the THz dynamics of a selected set of liquid metals, all characterized by a melting point close to RT, namely Hg, Ga and $Li(NH_3)_4$. Hg and Ga have a demonstrated impact in technological applications while there is a potential for the stable phases of lithium-ammonia solutions, like $Li(NH_3)_4$. Knowledge of the dynamical response at THz frequencies of these systems could have an impact on applications that exploit their thermodynamics properties or the high-frequency waves propagation.

## 3. Inelastic neutron scattering in liquids

The theory of thermal neutron scattering from matter is described in several excellent textbooks [1,2] and review papers. Here, only the fundamental relationships useful to describe the liquid dynamics in the THz range are recalled.

The kinematic region accessible by the neutron probe is defined by the energy and momentum conservation laws during the scattering process, that is:

$$\epsilon_0 - \epsilon_f = \hbar\omega \qquad \mathbf{k}_0 - \mathbf{k}_f = \mathbf{q}$$

where $\epsilon_0 = (\hbar^2 k_0^2)/(2m)$ is the energy of the incoming neutron with wavevector $\mathbf{k}_0$ and $\epsilon_f = (\hbar^2 k_f^2)/(2m)$ the energy of the scattered neutron with wavevector $\mathbf{k}_f$. The scattering event is characterized by the energy transfer $\hbar\omega$ and the exchanged wavevector $\mathbf{q}$. Plots of the $(\hbar\omega, q)$ region typically accessible to the measurements are shown in Figure 2 for the two experimental configurations of a monochromatic incoming beam ($\epsilon_0$ = 80 meV)

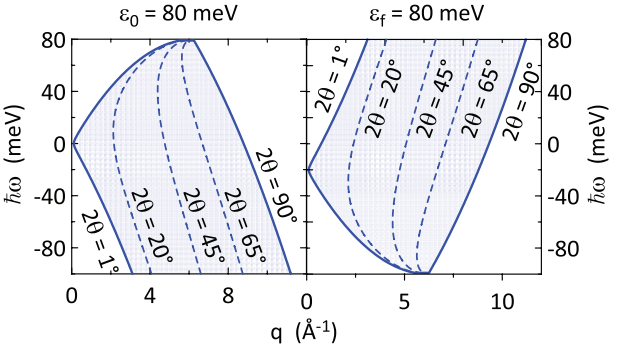


**Figure 2.** The kinematic regions of exchanged wavevector $q$ and energy $\hbar\omega$ accessible to the neutron scattering experiment with: fixed incoming neutron energy $\epsilon_0$=80 meV (left panel), and fixed scattered neutron energy $\epsilon_f$=80 meV (right panel). The different lines correspond to scattering angle configurations $2\theta$= 1°, 20°, 45°, 65°, 90°.

and a fixed final energy of the scattered neutron ($\epsilon_f$ = 80 meV), with the scattering angle $2\theta$ spanning from 1° to 90°.

The observable of the scattering process is the double-differential cross-section that, under the assumption of a weak coupling between neutron probe and system through a velocity-independent interaction potential, can be described within the Born approximation. The cross-section contains the excitation spectrum of the density fluctuations in the system embodied into the so-called dynamic structure factor $S(\mathbf{q}, \omega)$ [91]. As a consequence of the interaction with the neutron beam, the system, initially in the state $|\lambda_0\rangle$ makes a transition to the state $|\lambda_f\rangle$, with corresponding energies $E_{\lambda_0}$ and $E_{\lambda_f}$. The initial and final states of the system are defined by the isotopic distribution, the nuclear spin orientation, the position of the nuclei and, in magnetic materials, the orientations of the electron spin. The interaction potential coupling the external neutron with the nuclei of the system, neglecting the magnetic interaction that originates from the neutron spin, can be expressed very generally as

$$V(\mathbf{r}) = \sum_j V_j(\mathbf{r} - \mathbf{R}_j)$$

where $\mathbf{R}_j$ is the position of the $j$-th scattering nucleus. For unpolarised neutron beams, the cross-section can be written as

$$\frac{\mathrm{d}^2\sigma}{\mathrm{d}\Omega \mathrm{d}E_{\lambda_f}} \propto \frac{k_f}{k_0} \sum_{\lambda_0,\lambda_f} p_{\lambda_0} |\langle \lambda_f | \sum_j V_j(\mathbf{q}) \exp(i\mathbf{q} \cdot \mathbf{R}_j) |\lambda_0\rangle|^2 \delta(\hbar\omega + E_{\lambda_0} - E_{\lambda_f}) \tag{1}$$

where

$$V_j(\mathbf{q}) = \int \mathrm{d}\mathbf{r} \exp(i\mathbf{q} \cdot \mathbf{r}) V_j(\mathbf{r})$$

The sum in eq. 1 is taken over the final states $|\lambda_f\rangle$ and the initial states $|\lambda_0\rangle$ occurring with probability $p_{\lambda_0}$ that, at thermal equilibrium, is given by the proper distribution function at temperature $T$. The averaging procedure, indicated by the overline, concerns two independent averages, namely over the nuclear spin orientations and the isotopic distribution. Further handling of eq. 1 under the simplifying assumption of $V_j$ independent of $j$, which amounts to associate solely the same *average* scattering length to all the nuclei, provides the very compact expression.

$$\frac{\mathrm{d}^2\sigma}{\mathrm{d}\Omega \mathrm{d}E_{\lambda_f}} \propto \frac{k_f}{k_0} \overline{|V(\mathbf{q})|^2} S(\mathbf{q}, \omega)$$

where the dynamic structure factor $S(\mathbf{q}, \omega)$ is given by

$$S(\mathbf{q},\omega) = \frac{1}{2\pi}\int_{-\infty}^{\infty} \mathrm{d}t\, \exp(-i\omega t) \sum_{j,j'} \langle \exp[-i\mathbf{q}\cdot\mathbf{R}_j(0)]\, \exp[i\mathbf{q}\cdot\mathbf{R}_{j'}(t)]\rangle \quad (2)$$

The relationship of $S(\mathbf{q},\omega)$ with the density fluctuations of the system, namely with their excitation spectrum or equally their correlations at different times, is immediately evident by introducing the particle density operator $\rho(\mathbf{r},t)$ with Fourier components $\rho_{\mathbf{q}}(t)$, that is

$$\rho(\mathbf{r},t) = \sum_j \delta(\mathbf{r}-\mathbf{R}_j(t)) \qquad \rho_{\mathbf{q}}(t) = \sum_j \exp[-i\mathbf{q}\cdot\mathbf{R}_j(t)]$$

which enables expressing eq. 2 as

$$S(\mathbf{q},\omega) = \frac{1}{2\pi}\int_{-\infty}^{\infty} \mathrm{d}t\, \exp(-i\omega t) \langle \rho_{\mathbf{q}}(0)\rho_{-\mathbf{q}}(t)\rangle \quad (3)$$

The cross-section observable in the scattering experiment with unpolarised neutrons can therefore be simply cast as the product of a term related to the probe-target interaction potential in $\mathbf{q}$-space, $V(\mathbf{q})$, by the dynamic structure factor $S(\mathbf{q},\omega)$ that is a density-density response function. The nature of the response originates from the neutron probe coupling to the system density fluctuations [97] and depends on the target properties only, as a consequence of the linear response regime treatment of the scattering process. The assumption on the neutron–nucleus interaction potential as independent of the single nucleus, which simplifies the average over the isotopes and the nuclear spin, amounts to calculate the so-called coherent contribution to the cross-section and eqs. 2 and 3 represent the coherent dynamic structure factor that is also measured by x-ray inelastic scattering [52]. When correctly accounting for the nuclei distributions, the averaged term $\overline{V_j^+(\mathbf{q})V_{j'}(\mathbf{q})}$ consists of the coherent contribution plus a second, incoherent, contribution that substantially describes the fluctuations of the scattering length around the average value. In summary, the neutron cross-section of $N$ scattering centres is given by the sum of the coherent and the incoherent terms, i.e.

$$\left(\frac{\mathrm{d}^2\sigma}{\mathrm{d}\Omega \mathrm{d}E_{\lambda_f}}\right)_{coh} = N\frac{k_f}{k_0}\frac{\sigma_c}{4\pi\hbar}S(\mathbf{q},\omega)$$

and

$$\left(\frac{\mathrm{d}^2\sigma}{\mathrm{d}\Omega \mathrm{d}E_{\lambda_f}}\right)_{inc} = N\frac{k_f}{k_0}\frac{\sigma_i}{4\pi\hbar}S_{inc}(\mathbf{q},\omega)$$

where $\sigma_c = 4\pi\overline{b}^2$ and $\sigma_i = 4\pi[\overline{b^2} - \overline{b}^2]$, $b_j$ the scattering length of the $j$-th nucleus and

$$S_{inc}(\mathbf{q},\omega) = \frac{1}{2\pi}\int_{-\infty}^{\infty} \mathrm{d}t\, \exp(-i\omega t) \sum_j \langle \exp[-i\mathbf{q}\cdot\mathbf{R}_j(0)]\, \exp[i\mathbf{q}\cdot\mathbf{R}_j(t)]\rangle \quad (4)$$

Some general rules are obeyed by $S(\mathbf{q},\omega)$ and $S_{inc}(\mathbf{q},\omega)$ as properties characteristics of the response functions. For instance, time causality implies the response function being an analytic function in one half of the complex $\omega$ plane. The first two $\omega$ moments of the dynamic structure factor exist and are expressed by

$$\int_{-\infty}^{+\infty} S(\mathbf{q},\omega)\, d\omega = S(\mathbf{q}) = 1 + n_i \int d\mathbf{r}\, [g(\mathbf{r}) - 1]\ \exp[i\mathbf{q}\cdot\mathbf{r}]$$

$$\int_{-\infty}^{+\infty} S_{inc}(\mathbf{q},\omega)\, d\omega = 1$$

$$\int_{-\infty}^{+\infty} S(\mathbf{q},\omega)\, \omega\, d\omega = \frac{\hbar q^2}{2M} = \int_{-\infty}^{+\infty} S_{inc}(\mathbf{q},\omega)\, \omega\, d\omega$$

where $S(\mathbf{q})$ is the static structure factor directly related to the pair correlation function $g(\mathbf{r})$, with $n_i$ the atomic (ionic) number density and $M$ the atomic mass. A general analysis based on the equation of motion for the density operator $\rho(\mathbf{r},t)$ shows that the dynamic structure factor can be developed as a continuous fraction with coefficients related to the moments [98,99]. This approach, although formally quite solid, has limited application in the interpretation of the experimental data.

A very useful development for the incoherent cross-section can be obtained in isotropic and homogeneous systems, which is independent of the structural disorder and exploits the harmonic oscillator model to describe the system dynamics. Starting from eq. 4, the $q$-dependent exponentials can be developed as a power series in the small $q$ limit, to obtain

$$S_{inc}(\mathbf{q},\omega) = \frac{1}{2\pi}\int_{-\infty}^{+\infty} dt\, \exp[-i\omega t] \left\{ 1 + \sum_j \langle [\mathbf{q}\cdot\mathbf{R}_j(0)]\, [\mathbf{q}\cdot\mathbf{R}_j(t)]\rangle + \ldots \right\}$$

where dots indicate higher order terms. The assumption of isotropic and homogeneous system allows to write

$$\begin{aligned} \langle [\mathbf{q}\cdot\mathbf{R}_j(0)]\, [\mathbf{q}\cdot\mathbf{R}_j(t)]\rangle &= \sum_{\alpha\beta} q^\alpha q^\beta \langle [R_j^\alpha(0)\, R_j^\beta(t)]\rangle \\ &= \sum_{\alpha\beta} \delta_{\alpha\beta}\, q^\alpha q^\beta \langle [R_j^\alpha(0)\, R_j^\alpha(t)]\rangle \end{aligned}$$

where $\alpha$ and $\beta$ indicate Cartesian coordinates and $\langle [R_j^\alpha(0)\, R_j^\alpha(t)] \rangle$, because of isotropy, does not depend on $\alpha$. Making use of this result, the incoherent dynamic structure factor can be written as

$$S_{inc}(\mathbf{q},\omega) = \frac{1}{2\pi}\, q^2 \int_{-\infty}^{+\infty} dt\, \exp[-i\omega t] \left\{ \sum_j \langle [R_j^\alpha(0)\, R_j^\alpha(t)] \rangle + \dots \right\}$$

where the time Fourier transform of $\langle [R_j^\alpha(0)\, R_j^\alpha(t)] \rangle$ contains the whole set of frequencies characteristic of the system, and hence the frequency spectrum. With some further math, the incoherent dynamic structure factor for a monatomic system, over the low $q$ region, results [1]:

$$S_{inc}(q,\omega) = \frac{\hbar^2 q^2}{2M}\, \exp[-2W(q)]\, \frac{g(\omega)}{\hbar\omega} [n(\omega)+1] + \mathcal{O}(q^4) + \mathcal{O}(q^6) \dots \quad (5)$$

where $g(\omega)$ represents the frequency spectrum of the system, and is an analogous of the phonon density of states in crystals, $n(\omega)$ is the Bose distribution function and $\exp[-2W(q)]$ is the Debye-Waller factor.

The value of the polynomial development of $S_{inc}(q,\omega)$ in powers of $q^2$ as given by eq. (5) is in its exploitation to get the density of states $g(\omega)$ by extrapolating the measured incoherent dynamic structure factor to zero wavevector. Indeed, the first, quadratic term provides the correct extrapolation to zero wavevectors as the higher terms become vanishingly small in this limit. It is worth mentioning that $g(\omega)$ is contributed by all the atomic vibrational modes at a given frequency $\omega$ independently of the mode character, differently from coherent scattering in crystals where precise selection rules control the cross-section that is proportional to $|\mathbf{q}\cdot\mathbf{e_q}|^2$, $\mathbf{e_q}$ being the eigenvector. This selection rule produces visibility of the modes with a finite component of the eigenvector along the wavevector transfer direction. In incoherent scattering from an isotropic system this effect is averaged out and the simpler expression in eq. 5 is obtained.

## 4. Polarisation analysis in non-magnetic systems

In disordered systems, disentangling the coherent from the incoherent term in an ordinary experiment is typically left to the data reduction and analysis that, in the case of neutron techniques, is quite sophisticated as built over more than 70 years of experimental practice. However, to fully exploit the richness of information carried by the inelastic neutron cross-section in liquids, polarisation analysis is the way at future high flux sources. Indeed, exploiting the cross-section dependence on the known polarisation of the incoming beam, and analysing the polarisation of the scattered beam as resulting from the interaction with the target system, has a proven potential for distinguishing the incoherent contribution in the scattering process,

although exploitation has been limited until now by the intensity *cost*. A limitation that can be overcome by the expected higher performances of a source like the ESS.

While the traditional area where neutron polarisation option offers unparalleled capability is the analysis of magnetic materials structure and dynamics [100–103], the application of this technique to the study of disordered non-magnetic systems remains largely unexploited. Indeed, if magnetic order is present, e.g. ferromagnetism, antiferromagnetism and other more complex spin alignments, the polarisation dependence of the cross-section is a unique tool to single out the magnetic response of the sample. However, some recent examples show the impact of polarised neutron scattering on the study of non-magnetic systems like water [35,36] or the analysis of collective excitations in liquid gallium [104], while the possibilities opened by this technique for the investigation of biological and hydrogen-containing systems are reviewed in [105].

The theory of polarisation analysis is reported in several textbooks [1]. Here we recall the major conclusions that applies to the case of neutron scattering from nuclei. The polarisation of a neutron beam is currently defined [1,22,26] by the polarisation vector given by $\mathbf{P} = 2\langle \mathbf{s}_n \rangle$, $\langle \mathbf{s}_n \rangle$ being the average neutron spin, and for the neutron-nuclei interaction process, it is found that: *a*) the nuclear coherent scattering is independent of polarisation and the polarisation of the outgoing beam is not affected by the coherent interaction with the sample nuclei; *b*) the incoherent contribution arising from the random isotope distribution of the sample is also independent of the polarisation that remains unchanged; and, finally, *c*) the incoherent scattering brought about by the random orientations of the

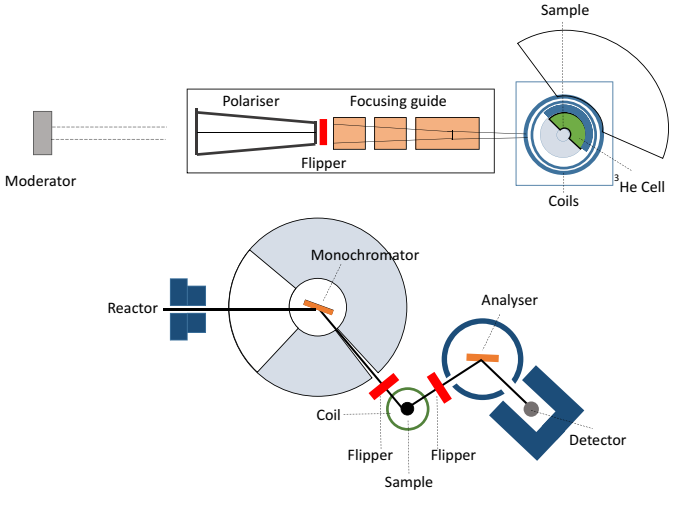


**Figure 3.** Schematics of a neutron instrument for inelastic scattering with polarisation analysis at a spallation source (upper panel) and a reactor source (bottom panel).

nuclear spins coupling to the neutron spin causes a spin flip of the polarised incoming beam and the polarisation of the scattered beam is then reversed (spin-flip) with a magnitude equal to one-third of the incoming one. Conceptually, the experiment requires the capability of measuring and changing the polarisation state of the incoming and scattered neutron beams, in addition to energies and wavevectors, and, since the first experimental setup [25], extraordinary progresses have been achieved in the techniques to produce and analyse the neutron polarisation [32,38,106]. The experiment typically consists in separately measuring the cross-section with and without spin-flip, which, for the neutron–nucleus interaction, enables to isolate the incoherent contribution originating from the disorder of the nuclear spin orientations. Figure 3 shows a schematics of the experimental setup for a polarised inelastic instrument at a pulsed neutron source (upper panel) and a 3-axes spectrometer at a reactor source (bottom panel).

Typically, beam polarisation is ignored in standard neutron scattering experiments, and an average over the incoming and outgoing beam polarisations is carried out. However, when the incoming neutron beam, prepared in a defined spin state, is scattered by nuclei having non-zero spin $I$, the coupled system can be found in two different final states, namely $|+\rangle = |I + 1/2\rangle$ and $|-\rangle = |I - 1/2\rangle$. The nuclear scattering length associated to these two states, $b_+$ and $b_-$, is not the same and, in the special case of hydrogen nucleus, that is the proton, there is even a change of sign. When there is no preferred nuclear spin orientation, as in systems at temperatures greater than ~1 mK, the neutron-nucleus coupling must be averaged over the nuclear spin states. The two relevant averages have to be considered,

$$\overline{b} = \frac{(I+1)b_+ + Ib_-}{2I+1} \qquad \overline{b^2} = \frac{(I+1)b_+^2 + Ib_-^2}{2I+1}$$

When $I = 0$, it follows $\overline{b} = b_+ = b_-$ and $\overline{b^2} = \overline{b}^2$, so there is no contribution from nuclear spin to the incoherent scattering that now originates from the isotope distribution only and is independent of the neutron polarisation.

The effect of measuring the polarisation dependent cross-section is clearly illustrated by elastic scattering in a Bravais crystalline sample in absence of magnetic contribution. Assuming the incoming beam polarisation $\mathbf{P}_0$ defined and the scattered beam polarisation $\mathbf{P}$ analysed, the measured polarisation dependent elastic cross-section is given by

$$\mathbf{P}\,\frac{d\sigma}{d\Omega} = \mathbf{P}_0 \left| \sum_i \exp[i\mathbf{q}\cdot\mathbf{R}_i]\,\overline{b} \right|^2 - \frac{1}{3}\mathbf{P}_0 N(\overline{b^2} - \overline{b}^2)$$

This relationship shows that the incoherent contribution gives rise to a spin-flip process with $\mathbf{P} = -1/3\mathbf{P}_0$. Therefore, the incoherent scattering of a fully polarised neutron beam produces a scattered beam where two-third of the scattered neutrons changed spin state and one-third remained in the original state. This result can be used to distinguish the coherent scattering cross-section from the incoherent (nuclear spin) contribution. For a sample containing several isotopes, the incoherent neutron scattering does not produce any spin flip.

These results are also exploited to obtain *clean* coherent and incoherent dynamic structure factors. The simplest example is the inelastic scattering in an elemental liquid sample made of a single isotope species with a given spin [24]. Coherent and incoherent terms can be obtained by carrying out two measurements of the inelastic cross-section in a configuration of a fully polarised incoming neutron beam ($\mathbf{P}_0 = \tilde{z}$) with the polarisation analysis of the scattered beam for non-spin flip ($++$ or $--$) and spin flip ($+-$ or $-+$) processes, that is $\mathbf{P}$ with the same or the opposite direction as $\mathbf{P}_0$, respectively. Assuming ideal beam polarisations, the cross-sections are given by

$$\left.\frac{\mathrm{d}^2\sigma}{\mathrm{d}\Omega \mathrm{d}E_{\lambda_f}}\right|_{++} = \frac{k_f}{k_0}\left[b^2\, S(q,\omega) + \frac{1}{3}\,\frac{\sigma_i}{4\pi}\, S_{inc}(q,\omega)\right]$$

and

$$\left.\frac{\mathrm{d}^2\sigma}{\mathrm{d}\Omega \mathrm{d}E_{\lambda_f}}\right|_{+-} = \frac{k_f}{k_0}\,\frac{2}{3}\,\frac{\sigma_i}{4\pi}\, S_{inc}(Q,\omega)$$

The study of collective excitations in liquid metals enjoyed considerable momentum almost 20 years ago thanks to the novel instrumentation for inelastic x-ray scattering installed at advanced photon sources like the ESRF [52], which led to notable advances in the description of the liquid system dynamics. The perspective today for making still another jump in the understanding of the complex liquid dynamics could come from polarised neutron studies at high brilliance sources, which have the potential of measuring simultaneously the coherent and the incoherent density-density response function, thus giving access to both the spectrum of density fluctuations and the single particle diffusion processes.

A full polarisation analysis experiment implies to carry out not less than 6 independent measurements of the inelastic cross-section with high statistics ($\sim$ 1–2%), which amounts to devoting a considerable beam time effort to a single experiment. For most of the presently installed spectrometers, neutron fluxes available at the sample enable

performing the investigations, although that would impact on the total number of experiments on the given beamline, due to the time-consuming scheme for the polarisation analysis measurements with only half of the incoming neutron flux selected (ideal polarisation efficiency). Therefore, a substantial increase of the flux at the sample would proportionally reduce the time duration of the experiments making them more accessible to a larger number of users. As an example, the performances expected by the new bi-spectral T-REX spectrometer with full polarisation analysis, to be installed at ESS, anticipate an intensity at the sample ranging from 5 to 50 times higher than at the existing spectrometers of the same class [107]. The flux gain also improves the signal-to-noise ratio by a factor equal to the square root of the scattered intensity at fixed collection time. Such a ratio is further improved by the increased sample distances from the neutron source [107]. These figures are critical to separate, by polarisation analysis, the coherent and incoherent scattering contributions for most isotopes where the typical $\sigma_i/\sigma_c$ ratio is below 10%. Therefore, apart from the shorter experimental time, hence the larger number of possible investigations, and the improved signal-to-noise ratio, the increased flux makes possible experiments where, at present, the polarisation analysis is difficult.

## 5. Collective excitations measured in liquid metals. Experimental characterization of the THz dynamics

The focus on liquid metals concerns the ability to describe the dynamic response in the regime $\omega\tau > 1$, where traditional hydrodynamics does not work, and to interpret the $\omega$ *vs* $k$ dispersion and the $\omega$-, $k$-dependent damping of long-living collective excitations, which are observed in a variety of thermodynamic states. A major issue is the actual complexity of the measured dispersion relations that, thanks to the increased experimental resolution and intensity and the remarkable improvements brought in by the x-rays techniques, results in more than just one longitudinal mode even in simple monatomic liquids. These features remind the behaviour of solids where they are completely understood as phonons in crystals. The additional trait, typical of liquids, is the diffusive particle motion that shows up in the response function and does not have a comparable counterpart in crystalline solids.

The Generalized Collective Modes (GCM) method [108,109] is a widely applied theoretical approach to the investigation of collective modes in liquids and an effective framework to analyse the transverse excitations spectra in liquids [110–113], binary mixtures [114,115] and glasses [116]. Also, the recent extensive molecular dynamics simulation work of Del Rio

et al. on liquid metals contribute to shed light on the interpretation of the vibrational spectra and the complex behaviour of collective modes in these systems [117–119].

Without entering the debate on the merits of the best theoretical approach describing the characteristic behaviour of the liquid, whether generalized hydrodynamics or a solid-like vibrational approach, for which the reader can refer to more specialised literature, we adopt the prescription emerging from recent papers published on the subject [60], which amounts to approximate properties in the liquid state related to system energy or specific heat, by using solid-like predictive models [58–61]. This statement is based on the demonstration that the energy and specific heat in a liquid are mostly contributed by the vibrational collective modes term, as in solids, which is dominant over the diffusive motion term. Further background to that, is the renewed interpretation of the Frenkel proposal of a liquid relaxation time as the average time between the diffusive jumps, that is, within this picture, particles in a liquid perform oscillations which resemble vibrations in a solid, for a certain time duration beyond which they jump diffusively to a nearby quasi-equilibrium position [60]. The assumption that at times smaller than the relaxation time the liquid dominantly behaves like a solid, unsurprisingly supports the prediction of transverse modes in addition to the longitudinal acoustic mode. Quite generally the combined view of the liquid dynamics made of solid-like vibrations and diffusive motions provides practical recommendations for modelling the collective dynamics and diffusion observed at Thz frequency and interatomic length scale in many liquids including liquid metals [77–82].

When discussing the possible presence of THz transverse modes in liquids, a key observation is the effective ability of the experimental technique to directly measure them. Indeed, by inelastic neutron or x-ray scattering, the coherent dynamic structure factor is observed, which, being a density-density correlation function, is contributed by the *longitudinal* density fluctuations only. In crystals, the presence of the reciprocal lattice allows to transfer part ($\mathbf{G}$) of the exchanged wavevector $\mathbf{q}$ to the lattice itself without energy transfer, that is $\mathbf{G} = \mathbf{q} - \mathbf{q}_{\mathrm{ph}}$ with $\mathbf{q}_{\mathrm{ph}}$ the phonon wavevector and $\mathbf{G}$ a reciprocal lattice vector, which makes the direct observation of transverse phonons possible. In liquids, the experimental *visibility* of transverse modes by neutrons or x-rays probes over this exchanged energy-wavevector region, depends on the hybridisation degree of transverse oscillations with the longitudinal sound.

As an example of what is measured in inelastic neutron and x-ray scattering experiments, Figure 4 shows a series of spectra collected in a few selected liquid metals, Rb [63], KCs [64], Ag [120], by neutrons (panel *a*) and Li [65], Na [78], Sn [82], by x-rays (panel *b*). The spectra

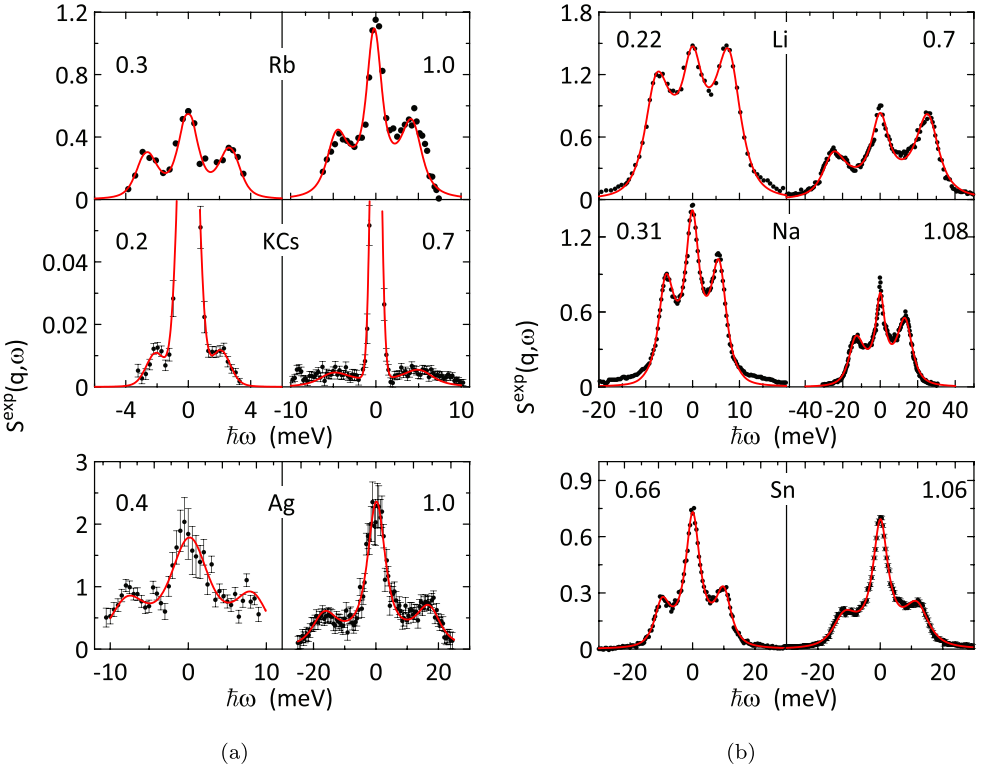


**Figure 4.** Dynamic structure factor of selected liquid metals versus exchanged energy. The experimental spectra of each sample are shown at the minimum and the maximum values of the measured wavevector transfer $q$, which are reported in the figures. Panel (a): neutron measurements in liquid Rb [63], KCs [64] and Ag [120]; panel (b): x-ray scattering in Li [65], Na [78] and Sn [82]. Experimental data are plotted as dots together with the errors shown when available. The full lines are the best-fitting curves obtained as the sum of a simple DHO plus a Lorentzian central peak.

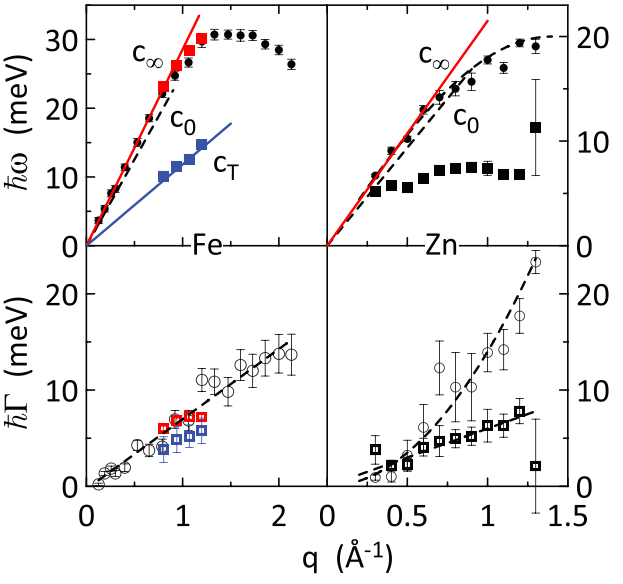


**Figure 5.** Dispersion relations (upper panels) and damping (lower panels) of the collective excitations measured in liquid Fe by x-ray scattering [80,121] and in liquid Zn [81] by neutron scattering. Two series of data are reported for liquid Fe: only the longitudinal mode (black symbols) is visible in the first series of data [80], while both longitudinal (red squares) and transverse (blue squares) modes are reported from [121]. Liquid Zn shows both longitudinal (circles) and transverse (squares) modes. The ordinary sound velocity $c_0$ and the fast sound $c_\infty$ associated to the longitudinal acoustic mode are plotted for both Fe and Zn. The transverse velocity $c_T$ is shown for Fe only.

are plotted versus energy and at selected values of the experimental wavevectors, with the aim of showing the characteristic features of the $S^{\mathrm{exp}}(\mathbf{q},\omega)$ function, in particular the triple-peak shape persisting with increasing the wavevector well beyond the hydrodynamic limit and up to almost the $q$-position of the first maximum of the static structure factor $S(q)$. In particular, the neutron data on Rb [63] and the x-rays data on Li [65] represent the first clear experimental evidence of propagating excitations over the THz region, which gave rise to further studies in the following years.

The analysis of the measured $S^{\mathrm{exp}}(\mathbf{q},\omega)$ data provides the dispersion relations $\omega_j(q)$ of the $j$-th mode, the modes damping and the value of the velocity associated with the mode, which is obtained by extrapolating $\omega_j(q)$ to $q \to 0$. As an example, the dispersion relations and the damping obtained by a neutron experiment in Zn [81] and by x-ray scattering measurements in Fe [80,121] are shown in Figure 5. The analysis is typically carried out using different fitting models to reproduce the inelastic structures, which can be generally grouped as empirical models based on the memory function approach [52,98,99] and conservation rules [122,123] or derived from a solid-like interacting-phonon model [81,124–126]. A review is given in

**Table 1.** Collective mode velocity. $c_0$ is the ordinary sound velocity obtained from [132] and $c_\infty$ the fast sound velocity associated with the longitudinal acoustic mode measured at THz frequency. $c_T$ is the velocity associated with a transversal acoustic mode after eq. 6. $c_{BS}$ is the Bohm-Staver approximation for the sound velocity, while $\Omega_p/k_s$ is an improved estimate of velocity with the correct expression for $k_s$ [89], and $c_{mod}$ is the collective-mode velocity of eq. 8 given by the full model described in [89].

| Element | $c_0$ (meV Å) | $c_\infty$ (meV Å) | $c_T$ (meV Å) | $c_\infty/c_0$ | $c_{BS}$ (meV Å) | $\Omega_p/k_s$ (meV Å) | $c_{mod}$ (meV Å) |
|---|---|---|---|---|---|---|---|
| Li | 29.95 | 36.5 ± 3.0 | 18 ± 9 | 1.219 | 44.58 | 29.00 | 26.50 |
| Na | 16.61 | 18.5 ± 1.0 | 7 ± 4 | 1.114 | 19.51 | 10.35 | 16.83 |
| K | 12.34 | 15.5 ± 1.0 | 8 ± 3 | 1.256 | 12.56 | 4.13 | 15.00 |
| Rb | 8.23 | 9.2 ± 0.5 | 3.6 ± 1.9 | 1.118 | 7.17 | 0.45*i* | 8.99 |
| Cs | 6.46 | 7.5 ± 0.4 | 3.3 ± 1.4 | 1.161 | 5.30 | 1.57*i* | 7.68 |
| Ca | 19.59 | 28.5 ± 2.0 | 18 ± 5 | 1.455 | 24.05 | 15.06 | 31.45 |
| Ba | 8.75 | 18.8 ± 2.0 | 14 ± 4 | 2.149 | 10.43 | 5.54 | 17.68 |

[127]. All these approaches contain, as the simplest approximation, the damped harmonic oscillator (DHO) model that has been applied to interpret the spectra of very diverse liquid systems. Indeed, the DHO fitting, in its simplicity and without striving to be a revealing theoretical tool, provides a guideline to figure out recurrent behaviours in alike and very different systems. Examples range from liquid water [73–75,128] to lithium-ammonia solutions [129]. We recall that DHO is formally obtained as the solution of the Langevin equation of the density fluctuations in the appropriate frequency limits, as reported in the experimental review [52] when discussing the generalized hydrodynamics based on the memory function formalism. Also, we observe that DHO is obtained as the weak-anharmonicity analytical limit of the phonon spectral density in anharmonic crystals [130,131].

As apparent from these figures, the velocity $c_\infty$ associated to the propagation of longitudinal density fluctuations, the so-called *fast sound*, can be derived by the linear extrapolation to $q \to 0$ of the dispersion curve, which typically is found to be higher than the values $c_0$ of the ordinary sound in the hydrodynamic regime. The experimental data of $c_\infty$ and $c_0$ [132] of the longitudinal mode are reported in Table 1 for liquid alkali and alkaline earth metals where the analysis presented in [89] is applied to calculate model values of the fast sound velocity.

The transition from slow to fast sound has been explained through different mechanisms either relaxation processes, typically described by generalized hydrodynamics or memory function approaches, or interactions directly included in the response function. The second picture relies on models like those based on the quasi-crystalline approximation [54,55,133] or related to interaction mechanisms between modes [81,124–126,134,135]. In the generalized hydrodynamics approach, a relationship is obtained for the elasticity moduli, which links the high frequency to the low-frequency

fluid dynamics [40,41] and is exploited in a formula connecting $c_0$ and $c_\infty$ to a velocity $c_T$ associated to the transverse modes [60], i.e.

$$c_0^2 = c_\infty^2 - \frac{4}{3}c_T^2 \tag{6}$$

The application of this formula has been questioned [136–138] as the *exact* use of the bulk and shear moduli depends on the precise identification of the low- and high-frequency regimes, and the formal description of the density fluctuations in liquids by generalized hydrodynamics [40] is subject to intense debate. Here, eq. 6 is applied to obtain an *experimental* guess at the velocity associated to the transverse modes possibly present in the liquid, by making use of the measured hydrodynamic sound velocity $c_0$ and the fast sound velocity $c_\infty$ provided by the extrapolation procedure of the experimental dispersion data. The $c_T$ values obtained for the liquid metals at the melting point are listed in Table 1 where also $c_0$ and $c_\infty$ are reported.

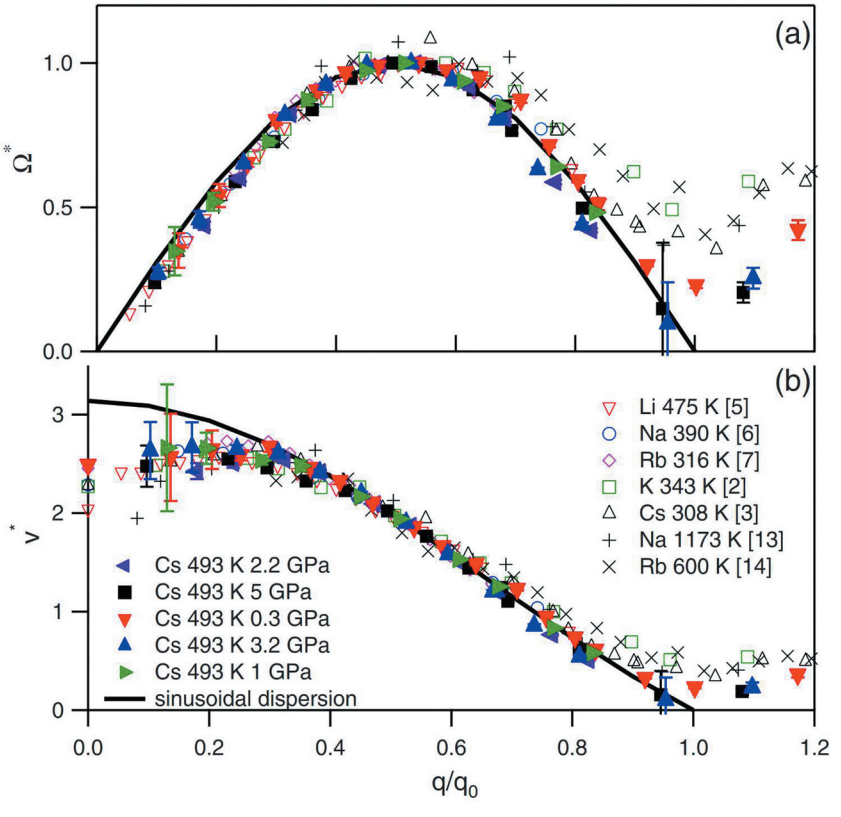


**Figure 6.** Data and curves from [140]. (a) Scaled dispersion curves and (b) sound velocity data for the alkali metals series. The q =0 values are the adiabatic sound velocities from Refs. [52] and [141]. The experimental data, according to the labelling indicated in panel (b) are from: Li 475 K [142], Na 390 K [143], Rb 316 K [63], K 343 K [144], Cs 308 K [145], Na 1173 K [146] Rb 600 K [147].

Whereas the challenge for a theory of liquids is to provide a general framework for the interpretation and the forward looking, a major ambition for the experiments is, through the fitting procedures, to identify common trends in the dynamics of liquid metals and possibly scale relations. Several attempts to recognise scaling behaviour in the dynamic properties have been done in the case of alkali metals although definitive conclusions have not been reached [52,53,64,88,139]. A most recent example of rescaling in liquid alkali metals is reported in Ref [140]. where a universal behaviour is found for the acoustic dispersion curves and the sound velocity over the wavevector range $0.15q_0 \leq q \leq 0.7q_0$, if plotted using the reduced units $q^\star = q/q_0$ and $\Omega^\star = \Omega/\Omega_0$ with $q_0$ the position of the main peak of the structure factor $S(q)$ and $\Omega_0$ the maximum of the dispersion curve. The validity of the proposed scaling is confined to the wavevector range above the hydrodynamic and below the single-particle regimes. The result of Ref [140]. is here reproduced in Figure 6.

Other attempts to facilitate a consistent interpretation of the THz dynamics of liquid metals have been done in a rather recent past [64,88,89] by casting the experimental data collected on alkali metals, alkali earths and polyvalent metals into a common frame founded on the theoretical treatment of the coupled electron-ion plasma [86,91,148]. Within the OCP (one component plasma) idealised model [149], liquid metals can be described as a system of charged particles, the ions, obeying the classical statistics and characterized by coupling constants that, at room temperature, are much greater than one (typically of the order of $10^2$ – $10^3$), which corresponds to a regime of strongly coupled plasma. Indeed, the coupling constant Γ is defined as the ratio of the average Coulomb energy to the average kinetic energy, that is

$$\Gamma = \frac{(Z_i e)^2}{a k_B T} = 2.69\text{x}10^{-5} Z_i^2 \left(\frac{n_i}{10^{12}\text{cm}^{-3}}\right)^{1/3} \left(\frac{T}{10^6\text{K}}\right)^{-1}$$

where the Coulomb energy per particle of the $N_i$ ions, each with an electric charge $(Z_i e)$, inside the volume $V$ is evaluated as $(Z_i e)/a$, with $a = [3V/(4\pi N_i)]^{1/3}$ the Wigner-Seitz radius of the sphere with $V/N_i = 1/n_i$ volume, and the kinetic energy per particle is approximated by $k_B T$. For a classical ion plasma, $Z_i \sim 1$ with typical densities $n_i$ of the order of $10^{22}\text{cm}^{-3}$, which provides $\Gamma \gg 1$ over the whole range of temperatures where the liquid metal exists and the ion system behaves like a classical strongly coupled plasma. The electrons, on the other hand, form a degenerate quantum plasma where the kinetic energy is approximated by the Fermi energy $E_F = \hbar^2 (3\pi^2 n)^{2/3}/(2m_e)$ of the gas with $m_e$ the electron mass and $n = Z_i n_i$ the number density related to the dimensionless Wigner-

Seitz radius of the electrons $r_s$ ($1/n = 4\pi r_s^3 a_0^3/3$, $a_0$ the Bohr radius). The coupling constant turns out to be

$$\Gamma_e = \frac{e^2}{r_s a_0 E_F} = 0.543\, r_s$$

where $r_s$ typically ranges between 2 and 6 for the conduction electrons in metals. Therefore, the conduction electrons of the liquid metal form a degenerate, strongly coupled plasma.

The ordinary treatment of the OCP assumes that the neutralizing charge, in this case the electrons that neutralize the average space-charge field of the ions, form a rigid, uniform background. This is a very simplified model that is more accurate in the limit of high electron density but rather limited to describe the properties of the liquid metal as a system of classical strongly coupled ions interacting with the quantum degenerate strongly coupled electron plasma that is a polarizable and not-rigid medium in the THz region. The bare ion-ion Coulomb interaction is indeed transformed into an effective short-range interaction because of the charge screening by the highly mobile electrons. In the approach of the linear response theory, the ion-ion dynamic screening effects are contained in the response function and specifically in the dielectric function $\epsilon(q,\omega)$ of the electron gas, which is approximated by its static limit $\epsilon(q,0)$ under the adiabatic decoupling of the electron and the ion motions. This is a reasonable approximation as the thermal energy of the ion motion is much lower than the Fermi energy of the electrons.

Actually, as pointed out in many reference studies since 1960 [87,90], liquid metals fit well within the description of a system of highly mobile conduction electrons interacting with the much heavier ions. Because of the electron–ion interaction, the electronic structure and the ion configuration, as well as the microscopic dynamics of both ions and electrons, are closely coupled and mutually dependent. The electron–phonon interaction is responsible for specific properties of metallic crystals, notably the superconductivity at low temperature. In the liquid phase of the metal, where the periodic structure of the lattice is lost, the simplest model is the plasma of dimensionless pointlike ions, charge-neutralised by the homogeneous interacting electron gas, and mutually interacting through the electron-screened ion-ion Coulomb interaction. This model, well known as the Bohm-Staver (BS) approach [91,150], supports the existence of collective modes of the ion plasma although neglecting the repulsive core potential, which amounts to emphasize the role of the electron density and electron-density-related effects against the ion size in governing the propagation of the ion density fluctuations. Indeed, the pointlike ions, moving in the otherwise homogeneous electron gas, induce a density fluctuation in the electron system, that

is a polarisation with a piling up effect of the electrons around the ionic charges, which, in turn, causes a screening of the bare Coulomb interaction among the ions and alters the frequencies associated to the propagation of the ion vibrations in the coupled electron-ion plasma. In the BS approximation, the frequency of the ion mode is given by

$$\omega^2(q) = \frac{\Omega_p^2}{\epsilon(q)} \tag{7}$$

where $\Omega_p$ is the ion plasma frequency, $\Omega_p^2 = 4\pi n_i (Z_i e)^2/M$, $M$ the ion mass. $\epsilon$(q) is the static dielectric function of the electron gas, which in the low $q$ limit and the Random Phase Approximation (RPA) is given by $\epsilon(q) \simeq 1 + k_{TF}^2/q^2$ with the inverse of the Thomas-Fermi wavevector $k_{TF}$ giving the size of the screening length. Under this scheme, the collective-mode velocity is obtained by taking the long-wavelength limit of eq. 7, that is

$$c_{BS} = \lim_{q\to 0} \frac{\omega(q)}{q} = \frac{\Omega_p}{k_{TF}} = v_F Z_i \sqrt{\frac{m_e}{3M}}$$

$v_F = (2E_F/m_e)^{1/2}$ the Fermi velocity.

Despite the crude approximation, the BS model provides an electron density-based scaling scheme via the dimensionless Wigner-Seitz radius of the electrons $r_s$ that reasonably accounts for the fast sound velocity trend in

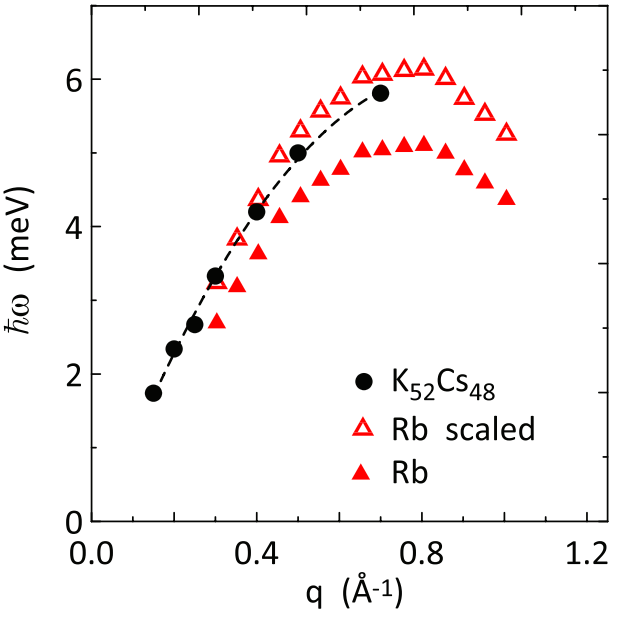


**Figure 7.** Dispersion relation of the collective longitudinal mode in $K_{52}Cs_{48}$ [64] (dots) compared with pure Rb (triangles) [63]. The dispersion relation of pure Rb after scaling by the effective alloy mass is also shown (empty triangles).

liquid alkali metals [64,89]. Actually, support to the electron density role as a scaling related parameter came from the study on collective excitations in the binary liquid system $K_{52}Cs_{48}$, whose composition was specifically chosen to match the $r_s$ value of pure Rb [64]. By taking into account the efiective mass of the alloy, a scaling of the dispersion curve of the alloy to that of Rb was obtained, which confirms that the electron density is a parameter sufficient to explain the scaling without resorting to the repulsive ion-core that is, indeed, very different in the two systems. The result of the scaling of the dispersion curves in heavy alkali metals, with the dielectric function, is shown in Figure 7.

Improved approaches over the BS scheme require removing the pointlike assumption on the ion size, including a better treatment of the electron-ion coupling as well as of the electron–electron interactions that play a major role at low electron densities (high $r_s$ values). Examples are given by the methodological approach presented in Ref [88]. and further bettered in Ref [89]. Both these studies are focused at identifying trends in the longitudinal collective mode velocity and damping and provide a model for comparison with the experimental data collected in a rather extended set of liquid metals. The key steps of the procedure beyond-BS are here summarised to report on the protocol described in [89], while a new detailed treatment of the coupled electron-ion system dynamics is given in the following section.

In the coupled electron-ion plasma, under the assumption of weak electron–ion interaction, which justifies a linear response theory approach, the frequencies associated to the propagating ion modes can be calculated self-consistently by solving the equation of motion for the amplitude associated to the ionic oscillations, with the system Hamiltonian expressed as the sum of three terms, namely purely ions, purely electrons and the electron–ion interaction term. The electron–ion interaction term is linear in the ion amplitude and contains the electron density fluctuations that are induced by the longitudinal field of the ion amplitude. The solution of the equation of motion provides the dispersion relation $\omega_R(q)$ of the *longitudinal* ion fluctuation density modes, i.e.

$$\omega_R^2(q) = \Omega^2(q) - \Omega_p^2 F(q) \left\{ 1 - \frac{1}{\epsilon[q, \omega_R(q)]} \right\}$$

where $\Omega(q)$ is the frequency of the normal modes of the ion plasma in absence of its coupling to the electrons, $F(q)$ the form factor of the ion–electron interaction potential and the dielectric function $\epsilon(q, \omega_R(q))$ of the electron gas can be replaced by its low frequency, low $q$ limit, that is $\epsilon(q, 0) \sim 1 + k_s^2/q^2$ with $k_s$ the electron gas screening wavevector. The velocity $c_{mod}$ of the collective modes is then obtained as

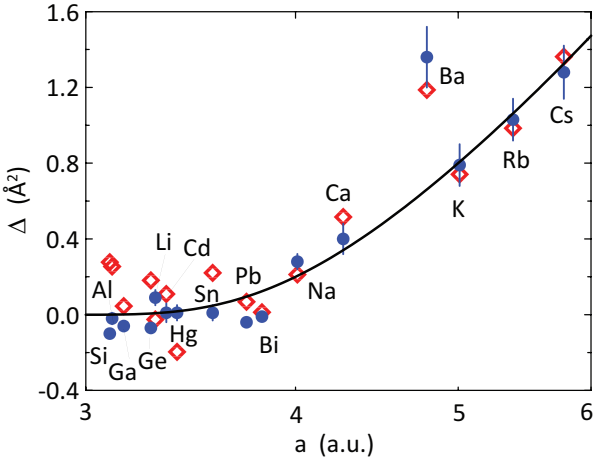


**Figure 8.** Velocity difference $\Delta$ versus the Wigner-Seitz radius $a$ of the ion sphere for a series of liquid metals. The data are plotted with a logarithmic $x$-axis scale to expand the lower values region. Experimental data (dots) are compared with the values calculated according to the model of eq. 8 (lozenges) and Ref [89]. The full line is a guide-to-the-eye.

$$c_{mod}^2 = \lim_{q\to 0} \frac{\omega_R^2(q)}{q^2} = \Omega_p^2 \left[ \frac{1}{k_s^2} + 2\frac{\delta_p}{q_D^2} + \frac{\langle R^2 \rangle}{6} \right] \tag{8}$$

by using the $q \to 0$ limit of $F(q)$ and $\Omega(q)$, that is

$$F(q) = 1 - \frac{\langle R^2 \rangle}{6} q^2 + \mathcal{O}(q^4) \qquad \Omega(q) = \Omega_p \left[ 1 + \delta_p \left( \frac{q}{q_D} \right)^2 + \mathcal{O}(q^4) \right]$$

with $q_D^2 = 4\pi n_i (Z_i e)^2/(k_B T)$ the Debye wavevector, $\delta_p$ a parameter entering the normal mode dispersion at small wavevectors [86] and $\langle R^2 \rangle$ the mean square radius of the electron–ion interaction potential. The knowledge of the ion charge $(Z_i e)$, the parameter $\delta_p$ and the size $\langle R^2 \rangle$ is sufficient to determine the velocity $c_{mod}$. In [89] a method is developed to calculate the density of the electron gas, and hence the ion charge $Z_i$, entering the dynamic response of the coupled plasma. The suggested protocol builds on the assumption that the relevant electron density in the process is the average electron density in the *interstitial* region, and that only the experimental structure of the liquid metal, i.e. the static structure factor $S(q)$, enters the determination of the electron density. The velocities of the longitudinal collective mode in alkali and alkaline earth liquid metals, calculated according to eq. (8) by applying the method proposed in [89], are reported in Table 1 in comparison with the experimental values $c_\infty$ obtained as the $q \to 0$ extrapolation of the measured collective-mode dispersion. Figure 8 shows a plot of the velocity difference $\Delta = (c_{mod}/\Omega_p)^2 - 1/k_s^2$ versus the Wigner-Seitz radius $a$ for the wider set of metals analysed in [89], in

comparison with the experimental estimates of the same quantity obtained using $c_\infty$. As apparent from Figure 8, $\Delta$ is a relatively smooth curve that accounts for all the data but Ba whose ratio $c_\infty/c_0$ also deviates remarkably from the trend shown by the other metals.

## 6. Self-consistent treatment of collective excitations in liquid metals. The interacting modes model

The fully quantum mechanical description of the liquid dynamics, thanks to the large $M/m_e$ mass ratio, can be reduced to the classical treatment of the ion dynamics under the adiabatic approximation with only the electrons being treated as quantum particles. A general starting point is the Hamiltonian of interacting electrons and ions, which first principle calculations in crystals rely on among which the very accurate lattice dynamics computations [151,152]. The Hamiltonian is given by the sum of the three terms related to purely ions $H_i$, purely electrons $H_e$ and electron–ion interactions $H_{ei}$, that is

$$H_i = \sum_j \frac{p_j^2}{2M} + \frac{1}{2}\sum_{jj'} U(\mathbf{R}_j - \mathbf{R}_{j'})$$

$$H_e = \sum_{\mathbf{k}} \frac{\hbar^2 k^2}{2m_e} c_{\mathbf{k}}^\dagger c_{\mathbf{k}} + \frac{1}{2}\sum_{\mathbf{k}\mathbf{k}'\mathbf{q}\neq 0} v_{\mathbf{q}} c_{\mathbf{k}+\mathbf{q}}^\dagger c_{\mathbf{k}'-\mathbf{q}}^\dagger c_{\mathbf{k}'} c_{\mathbf{k}}$$

$$H_{ei} = -\sum_{ij} W(\mathbf{r}_i - \mathbf{R}_j)$$

where $i$ and $j$ run over the electrons and the ions, respectively. The potentials $U(\mathbf{R})$ and $W(\mathbf{r},\mathbf{R})$ refer to the ion-ion and ion–electron interactions, and $v_{\mathbf{q}}$ is the Fourier transform of the bare Coulomb potential. A first evaluation of the electron term of the Hamiltonian is given by the mean field approximation for the electron–electron interactions, which results in

$$H_e = \sum_{\mathbf{k}} \epsilon(\mathbf{k}) c_{\mathbf{k}}^\dagger c_{\mathbf{k}}$$

where $\epsilon(\mathbf{k})$ is the effective single particle energy.

A physically appealing approach to the THz ion dynamics of a liquid, which recalls the relaxation time concept [40,60] to distinguish the liquid frequency regimes, should contain two major processes developing over quite different time scales, namely *slow* diffusion and *fast* density fluctuations caused by the vibrations around the instantaneous equilibrium positions $\mathbf{R}_j^{(0)}$. Within this *two time scale* approach the time-dependent ion positions, related to the local vibrations regime, can be written as

$\mathbf{R}_j(t) = \mathbf{R}_j^{(0)} + \mathbf{u}_j(t)$, as usual to describe phonons in crystals. To evaluate the density fluctuations caused by the ion displacements $\mathbf{u}_j(t)$ in the liquid, we first consider $H_i$ as the OCP Hamitonian for the strongly interacting ion plasma neutralized by the rigid negative uniform charge distribution, with $\mathbf{u}_j(t)$ developed using the normal mode description, i.e.

$$\mathbf{u}_j(t) = \frac{1}{\sqrt{N_i M}} \sum_{\kappa l} \mathbf{e}_{\kappa l} \exp[i\kappa \cdot \mathbf{R}_j^{(0)}] Q_{\kappa l}$$

where $\kappa$ runs over the reciprocal space and $l$ indicates the three vibrational modes. The three unit vectors $\mathbf{e}_{\kappa l}$ are mutually orthogonal and $Q_{\kappa l}$ is the amplitude operator. By substituting this canonical transformation into $H_i$, one gets

$$H_i = \frac{1}{2} \sum_{\kappa l} [P_{\kappa l}^{\dagger} P_{\kappa l} + \Omega_{\kappa l}^2 Q_{\kappa l}^{\dagger} Q_{\kappa l}]$$

where $P_{\kappa l} = \dot{Q}_{\kappa l}$ is the conjugate momentum of the coordinate $Q_{\kappa l}$ and $\Omega_{\kappa l}$ is the frequency of the OCP normal modes. In strongly coupled plasmas the frequency of the longitudinal mode $l = 1$ at $\kappa = 0$ is $\Omega_{0\,l=1}^2 = \Omega_p^2$.

The electron-ion term $H_{ei}$ contains the ion fluctuations $\mathbf{u}_j$ around $\mathbf{R}_j^{(0)}$ while the static contribution due to the instantaneous equilibrium positions $\mathbf{R}_j^{(0)}$ is included in the electronic term $H_e$ through the single-particle electron energies $\epsilon\mathbf{k}$. Substituting the normal mode description of $\mathbf{u}_j$ in $W(\mathbf{r}_i - \mathbf{R}_j)$, the Hamiltonian $H_{ei}$ is explicitly written in terms of the coordinate $Q_{\kappa l}$ and the Fourier transform of the electron density operator $\rho^e(\mathbf{r})$ where

$$\rho^e(\mathbf{r}) = \sum_i \delta(\mathbf{r} - \mathbf{r}_i) = \frac{1}{V} \sum_{\mathbf{k}\mathbf{k}'} c_{\mathbf{k}}^{\dagger} c_{\mathbf{k}'} \exp[i(\mathbf{k} - \mathbf{k}') \cdot \mathbf{r}]$$

After some manipulation [91,148], the Hamiltonian $H_{ei}$ becomes

$$\begin{aligned} H_{ei} &= -i \frac{1}{V} \sqrt{\frac{N_i}{M}} \sum_{\mathbf{k}\kappa} \kappa w_\kappa \langle 0 | c_{\mathbf{k}}^{\dagger} c_{\mathbf{k}-\kappa} | 0 \rangle Q_{\kappa l=1} \\ &= -i \frac{1}{V} \sqrt{\frac{N_i}{M}} \sum_{\kappa} \kappa w_\kappa \rho_{-\kappa}^e Q_{\kappa l=1} \end{aligned}$$

where $|0\rangle$ is the electron ground state with the ions in the instantaneous equilibrium positions, $w_\kappa$ is the Fourier transform of the electron-ion term $W(\mathbf{x})$ and $\rho_\kappa^e$ is the electron density fluctuation in reciprocal space. The result obtained for $H_{ei}$ shows that only the longitudinal mode $Q_{\kappa l=1}$ contributes, which derives from the gradient of $W(\mathbf{x})$ being parallel to $\kappa$. It is

usual to approximate $w_\kappa$ including a form factor $F(\kappa)$ accounting for the finite size of the ion core, that is $w_\kappa = 4\pi e^2 Z_i F(\kappa)/\kappa^2$.

Casting together the purely ionic term with the electron-ion coupling term, the Hamiltonian describing the fast vibrational dynamics in liquids is obtained as

$$\mathcal{H}_{ph} = \frac{1}{2}\sum_{\kappa l}\left\{[P^\dagger_{\kappa l}P_{\kappa l} + \Omega^2_{\kappa l}Q^\dagger_{\kappa l}Q_{\kappa l}] - i\,\frac{1}{V}\sqrt{\frac{N_i}{M}}\kappa\, w_\kappa \rho^e_{-\kappa}\, Q_{\kappa l=1}\right\}$$

with $\mathcal{H}_{ph}$ so-called because of the similarity with phonons in crystals. The electron density $\rho^e_\kappa$ can be related to the ion density $\rho_\kappa$ fluctuations at the frequency $\omega$ by the dielectric function through the following equation

$$\rho_\kappa = \frac{1-\epsilon(\kappa,\omega)}{\epsilon(\kappa,\omega)}\,\rho^e_\kappa$$

where the ion density fluctuation $\rho_\kappa$ is given, after some manipulation, by

$$\rho_{-\kappa} \simeq -i\sum_j \exp[-i\kappa\cdot\mathbf{R}^{(0)}_j]\,\kappa\cdot\mathbf{u}_j = i\sqrt{\frac{N_i}{M}}\kappa Q^\dagger_{\kappa l=1} \tag{9}$$

which, once more, clearly shows that only the longitudinal component $l = 1$ contributes to the ion density fluctuations. The final form of $\mathcal{H}_{ph}$ in terms of the coordinates $Q_{\kappa l}$ is then

$$\mathcal{H}_{ph} = \sum_\kappa\left\{\frac{1}{2}\sum_l[P^\dagger_{\kappa l}P_{\kappa l} + \Omega^2_{\kappa l}Q^\dagger_{\kappa l}Q_{\kappa l}] + \frac{n_i}{M}\,\kappa^2\, w_\kappa\,\frac{1-\epsilon(\kappa,\omega)}{\epsilon(\kappa,\omega)}\,Q^\dagger_{\kappa l=1}Q_{\kappa l=1}\right\}$$

The eigenvalues of this Hamiltonian must be obtained self-consistently with the frequency $\omega$ appearing in the electron-ion coupling. As such a procedure is quite cumbersome, a simple and most reasonable approximation is to assume a negligible frequency dependence for the dielectric function, that is $\epsilon(\kappa,\omega) \simeq \epsilon(\kappa,0)$ which in the limit of $\kappa \to 0$ is given as $\epsilon(\kappa,0) \simeq 1 + k_s^2/\kappa^2$. This specific approximation with the screening wave vector $k_s$ deduced from accurate electron gas calculations has been discussed in detail in [89] to compare calculated and experimental long-wavelength longitudinal collective-mode velocities of a wide set of liquid metals.

The $\mathcal{H}_{ph}$ Hamiltonian provides eigenvalues with a negligible imaginary part as the only contribution to the collective modes damping is due to the imaginary part of the dielectric function, which is very small in this energy limit ($\hbar\omega \ll E_F$). This is rather in disagreement with the experimental findings that show a notable mode damping over the kinematic accessible range. Indeed, an important contribution to the collective mode damping comes from the microscopic intrinsic disorder always present in a liquid

system [153]. Moreover, we remark that the Hamiltonian $\mathcal{H}_{ph}$ models a homogeneous and isotropic system, whereas at microscopic level the symmetry is spontaneously broken. To account for such an effect, additional terms have to be introduced in the Hamiltonian of the liquid system. Considering that in a disordered system no ordering of the eigenvalues with the momentum is possible, and that in the long wavelength limit the system modelling must reduce to the elastic continuum description, a quite reasonable approximation for the full Hamiltonian is given by [81,124–126],

$$\mathcal{H} \simeq \mathcal{H}_{ph} + \mathcal{H}_{int} + \mathcal{H}_a \tag{10}$$

where the first term describes the sum of 3 $N_i$ harmonic oscillators with oscillation frequencies given by the self-consistent eigensolutions of $\mathcal{H}_{ph}$. The second term introduces a linear mode-mode interaction to account for the symmetry breaking at atomic level and the consequent mode hybridisation, that is

$$\mathcal{H}_{int} = \frac{1}{2} \sum_{\kappa ll'} [U_{ll'}(\kappa) Q^{\dagger}_{\kappa l} Q_{\kappa l'} + hc]$$

while the third contribution $\mathcal{H}_a$ accounts for all the effects originating from the disorder of the system, which is expected to cause a remarkable damping of the vibrational modes at large $\kappa$.

The Hamiltonian in eq. 10 is then used to derive the dynamic structure factor $S(\mathbf{q}, \omega)$ in the *high-frequency sector* by applying the equation of motion for the specific Green's function [154]. To this purpose, $S(\mathbf{q}, \omega)$ can be conveniently written as the sum of contributions coming from the modes, that is

$$S(\mathbf{q}, \omega) = \sum_{ll'} \mathcal{F}_{ll'}(\mathbf{q})\, S_{ll'}(\mathbf{q}, \omega)$$

where $\mathcal{F}_{ll'}(\mathbf{q})$ is the mode structure factor that depends on the local structure of the liquid and [1]

$$S_{ll'}(\mathbf{q}, \omega) = -\frac{1}{\pi} [n(\omega) + 1] \Im \left\{ \int dt \, \langle\langle Q^{\dagger}_{\mathbf{q}l}(t); Q_{\mathbf{q}l'}(0) \rangle\rangle \, \exp[-i\omega t] \right\}$$

with $n(\omega)$ the Bose population factor and $\langle\langle Q^{\dagger}_{\mathbf{q}l}(t); Q_{\mathbf{q}l'}(0) \rangle\rangle = \mathcal{G}_{ll'}(\mathbf{q}, t)$ the Green's function given by

$$\mathcal{G}_{ll'}(\mathbf{q}, t) = -i\theta(t) \langle [Q^{\dagger}_{\mathbf{q}l}(t), Q_{\mathbf{q}l'}(0)] \rangle$$

As apparent, $\mathcal{G}_{ll'}(\mathbf{q}, t)$ is simply related to the correlation function $\langle Q^{\dagger}_{\mathbf{q}l}(t)\, Q_{\mathbf{q}l'}(0) \rangle$ and, through eq.9, to the density-density correlation

function. By solving the equation of motion for the Green's function $\mathcal{G}_{ll'}(\mathbf{q},t)$, that is

$$i\hbar\frac{d\mathcal{G}_{ll'}(\mathbf{q},t)}{dt} = \hbar\delta(t)\langle[Q^{\dagger}_{\mathbf{q}l}(t),Q_{\mathbf{q}l'}(t)]\rangle - i\theta(t)\langle[[Q^{\dagger}_{\mathbf{q}l}(t),\mathcal{H}],Q_{\mathbf{q}l'}(0)]\rangle$$

the mode-mode terms $S_{ll'}(\mathbf{q},\omega)$ are obtained as the $ll'$ element of the inverse matrix $\{\delta_{ll'}[\omega^2-\omega^2_{\mathbf{q}l}-\Sigma_l(\mathbf{q},\omega)]+U_{ll'}(\mathbf{q})\}^{-1}$, with $\Sigma_l(\mathbf{q},\omega)$ is the self-energy brought about by $\mathcal{H}_a$, which, although depending on the actual form of the Hamiltonian, has some defined properties, among which satisfying the Kramers-Kröning dispersion relations. The simplest form of $\Sigma_l(\mathbf{q},\omega)$, with the real part an even function and the imaginary part an odd function, is built as $\Sigma_l(\mathbf{q},\omega)\simeq i\Gamma(\mathbf{q})\omega$ where the imaginary part is proportional to $\omega$ and the real part is identically zero.

The dynamic structure factor $S(\mathbf{q},\omega)$ derived according to the described theoretical approach has been applied to model the data measured by the inelastic neutron-scattering experiment in liquids and disordered systems. In all cases this model has provided a very good description of the collective-mode dispersion relations and damping with the advantage of requiring a minimal number of parameters to be fitted on the experimental data.

## 7. Experiment and data analysis in three exemplary liquid metals: Hg, Ga and $Li_x(NH_3)_{1-x}$

The interacting modes model has been successfully applied to describe the features of coherent excitations observed in systems as different as glassy $SiSe_2$ [125] or molten Zn [81] and GeTe [126] or even DNA [155] powder and biological membranes [124]. In all these cases, the model had the value of pointing out at the presence of modes additional to the acoustic longitudinal mode, not excluding their transverse nature which can be observed through a mode hybridisation mechanism. Here, we discuss the two long-standing, as still debated, cases of liquid mercury and gallium whose vibrational dynamics has been investigated in diverse thermodynamic conditions using both neutron and x-ray scattering approaches. The interpretation of the inelastic features of either mercury or gallium contains open, unanswered questions that, we believe, the present interacting modes approach can contribute to resolve. The following analysis, here applied for the first time, offers a consistent framework for the experimental observations clarifying specific spectral features that had been interpreted resorting to less common explanations. Finally, we discuss the propagation of the longitudinal mode in lithium-ammonia solutions at different Li concentrations.

**Table 2.** Number density $n_i$ [156], Wigner-Seitz radius $a$, $r_s$ parameter, boiling ($T_b$) [157] to melting ($T_m$) [158] temperature ratio for a series of metals. The $r_s$ parameter is associated with the interstitial electron density, calculated as described in [89].

| Element | $n_i$ (at Å$^{-3}$) | $a$ (at. units) | $r_s$ | $T_b/T_m$ |
|---|---|---|---|---|
| Li | 0.0448 | 3.30 | 3.249 | 3.53 |
| Na | 0.0250 | 4.01 | 4.000 | 3.11 |
| K | 0.0128 | 5.01 | 4.903 | 3.11 |
| Rb | 0.0103 | 5.39 | 5.478 | 3.08 |
| Cs | 0.0083 | 5.78 | 5.904 | 3.19 |
| Ca | 0.0207 | 4.27 | 3.416 | 1.58 |
| Ba | 0.0147 | 4.79 | 3.997 | 1.91 |
| Al | 0.0536 | 3.11 | 2.204 | 2.94 |
| Si | 0.0541 | 3.10 | 2.064 | 2.09 |
| Ge | 0.0455 | 3.28 | 2.230 | 2.56 |
| Ga | 0.0511 | 3.16 | 2.248 | 8.82 |
| In | 0.0368 | 3.52 | – | 5.29 |
| Sn | 0.0354 | 3.57 | 2.454 | 5.69 |
| Cd | 0.0428 | 3.35 | 2.650 | 1.75 |
| Hg | 0.0410 | 3.40 | 2.451 | 2.69 |
| Tl | 0.0331 | 3.65 | – | 3.00 |
| Pb | 0.0308 | 3.74 | 2.557 | 3.36 |
| Bi | 0.0289 | 3.82 | 2.565 | 3.37 |

This is an extensively investigated system that keeps an unmodified interest under both the fundamental physics perspective, being a rare example of very low-density electron gas with a conjectured Kohn anomaly and an interesting Mott transition, and the potential for applications when in stable phase.

### 7.1. Mercury, a case study for liquid metals

Mercury is quite an interesting system with some peculiar characteristics like the lowest melting point of all the metals ($T_m$ = 234.28 K in normal conditions) and the highest number density of the heavy polyvalent metals, which is actually close to that of the much lighter Ga (0.0511 at/Å$^3$). These data are reported in Table 2.

Previous investigations of collective modes in liquid Hg [89,159,160] proved the existence of a transition from slow ($c_0$) to fast sound ($c_\infty$) with an experimental ratio $c_\infty/c_0 = 1.39 \pm 0.15$, which is in fair agreement with the prediction $c_\infty/c_0 = 1.330$ obtained evaluating the fast sound velocity by $\Omega_p/k_s$. This approximation represents a minimal step beyond Thomas-Fermi with the substitution of $k_{TF}$ by $k_s$, and it actually results from eq. 8 if assuming $F(q)\sim 1$ and $\Omega(q)\sim\Omega_p$ [89]. The observed agreement is rather surprising as the calculated ratio is obtained by substantially neglecting the ion size ($F(q)\sim 1$) in a system like the high-density liquid Hg with a relatively large size of the ion core. These characteristics of Hg, on the contrary, would suggest a sizeable contribution of the ion–ion interactions

not accounted for by the simple electron screening model in pointless ion plasma. Actually, the effect of the ion size, expressed by $\langle R^2 \rangle$ in eq. 8, is largely cancelled out by the ion plasma dispersion, embodied in the parameter $\delta_p$ that results to be negative in mercury [86], which explains why the relatively simple calculation of the velocities ratio agrees with the experimental findings. This explanation was not offered at the time of the investigations in [159,160] and the dynamics of liquid Hg appeared to be mostly driven by the electron screening as in liquid alkali metals.

Further to that, both the neutron scattering experiment [159] and the x-ray measurement [160] in liquid Hg reported the observation of a consistent broadening of the quasi-elastic peak which could not be attributed to free diffusion only. This feature of the experimental spectra was interpreted as a quasi-elastic contribution originating from a fast, rattling mechanism of the atoms inside the local cage and accompanying the usual slower free diffusion of the atoms in real space. This interpretation was complemented by computational work [161–164] that attributed the broaden quasi-elastic structure to self-dynamics (single particle) processes, although it remained a somewhat controversial point [164,165]. A better grasp on the liquid mercury dynamics would come from experiments with a much improved energy resolution, despite some limitations intrinsic to the techniques which cannot be easily overcome. Indeed, the energy resolution of the neutron-scattering experiment in [159] was Gaussian-like with 1.16 meV full width at half maximum (FWHM), while it was an almost-Lorentzian function with 2.15 meV FWHM in the x-ray experiment [160]. These relatively coarse values of energy resolutions were obtained by pushing the performances of the top-level three-axis spectrometer IN1 at the ILL (Grenoble, FR), and using the 3-ID-C beamline at the Advanced Photon Source of the Argonne National Laboratory (Illinois, USA).

To clarify the nature of the broad quasi-elastic peak in Hg, an additional, new experiment was carried out using the high resolution, long wavelength, IN5 spectrometer at the ILL. A very thin (0.1 mm) hollow cylindrical sample, maintained at $T = 245$ K, was measured at 5.113 Å incoming neutron wavelength with a Gaussian-like energy resolution equal to 0.22 meV on the elastic line. Obtaining a thin sample was a critical requirement dictated by the high neutron capture cross-section of Hg, which increases proportionally to the neutron wavelength $\lambda$. The dynamic range associated to the IN5 configuration was not suited to study collective excitations in liquid mercury, as the neutron velocity ( $\simeq$ 775 m/s) was smaller than the sound velocity (1451 m/s) and the longitudinal acoustic mode could not be observed by coherent scattering at low wavevectors transfer. The IN5 experiment was tailored to measure the incoherent inelastic cross-section of Hg for obtaining the density of states, which is

a companion information of the collective-mode dispersion provided by coherent neutron and x-ray experiments. This was facilitated by the high incoherent cross-section of mercury. Furthermore, mercury is a particularly fortunate case for the analysis of the incoherent cross-section: indeed, the contribution of the coherent cross-section was negligible, namely $S(q) < 0.1$ at $q < 1.7$ Å$^{-1}$, and could be disregarded when extrapolating the cross-section to $q = 0$ to obtain the density of states, as described in eq. 5. The experimental resolution was rather good but still broader than needed for a study of the shape of the quasi-elastic peak, considering the value of the self-diffusion coefficient $D \simeq 1\,10^{-5}$ cm$^2$ s$^{-1}$ at the melting point [166,167].

As a general remark, experiments aimed at obtaining the density of states in liquids by measuring the incoherent inelastic scattering directly are rather difficult because the incoherent cross-section of the sample is typically not sufficiently large. These ordinary cases could be beneficially investigated by using polarisation analysis on high-performance sources where the effect of low incoherent cross-section of the sample would be compensated by an incoherent-selective technique.

Here we re-analyse the data of both neutron [159] and x-ray [160] scattering at low momentum making use of the interacting mode model described in the previous section, jointly with the analysis of the new incoherent scattering neutron data applied to determine the Hg density of states. Bringing together coherent and incoherent data, within the framework of the interacting modes model for the collective excitations, is a powerful tool that enables to obtain a consistent picture of the atomic dynamics in mercury close to the melting point. The experimental, coherent, dynamic structure factors obtained from the neutron experiment in [159] and the x-ray one in [160] were considered as a unique data set and simultaneously analysed, that is using, at the *same time*, the *same model function* with the *same parameters* for both the experiments, apart from different scale factors. A different treatment of the quasi-elastic term was applied because the strong incoherent contribution in the neutron data is absent in x-ray scattering. The strong quasi-elastic peak due to incoherent scattering of Hg tends to obscure the purely inelastic features of the spectra making the collective dynamics measurement difficult, despite the short-tailed Gaussian-like resolution function of the neutron experiment. However, a large incoherent cross-section is a useful characteristic when designing the experiment aimed at the determination of the density of states.

We modeled the coherent dynamic structure factor $S(q, \omega)$ applying the interacting mode model with two modes, that is

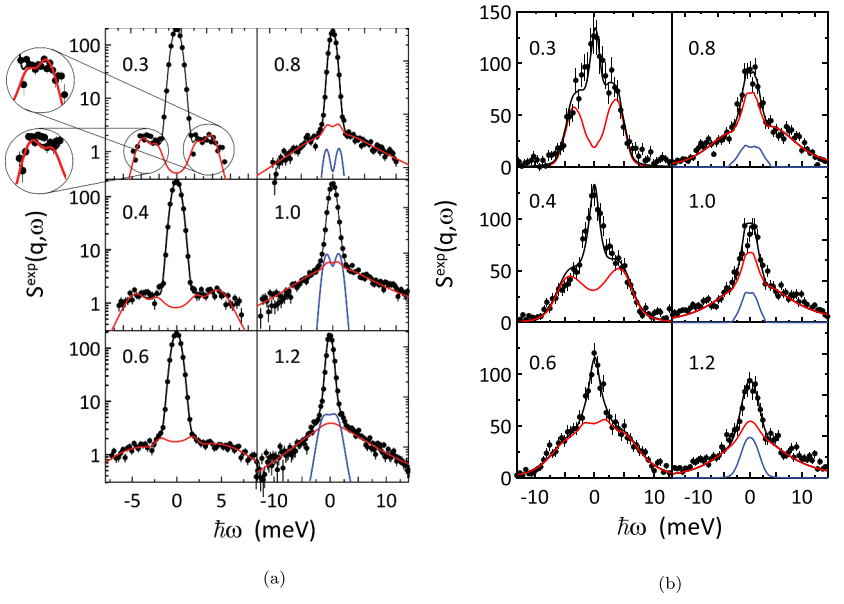


**Figure 9.** Experimental dynamic structure factor of liquid Hg versus exchanged energy, at the different values of the measured wavevector transfers $q$. Panel (a): neutron measurements [159]; panel (b): x-ray scattering [160]. The neutron spectra are plotted on log-scale to emphasize the inelastic features. The black full lines are the best-fitting curves obtained by the interacting modes model limited to 2 modes. Contribution from mode "1": red line; contribution from mode "2": blue line. The enlarged view of the top left spectrum in panel $(a)$ shows the ability of the model to reproduce details of the lineshape.

$$S(q,\omega) = \sum_{l=1,2} A_l(q)\, S_{ll}(q,\omega)$$

where $A_l(q)$ is a scale factor and the mode-mode dynamic structure factors $S_{ll}(q,\omega)$ are given by the diagonal terms of the matrix

$$S_{ll}(q,\omega) = \{\delta_{ll'}[\omega^2 - \omega_{ql}^2 - \Sigma_{ql}(\omega)] + U_{ll'}(\mathbf{q})\}^{-1}_{ll}$$

Here $\omega_{ql}$ $(l = 1, 2)$ stands for the mode frequencies and $\Sigma_{ql}(\omega)$ is the corresponding self-energy approximated by $\Sigma_{ql}(\omega) \simeq i\Gamma_{ql}\omega$, as the simplest form satisfying the Kramers-Kröning dispersion relations. This approximation for $\Sigma_{ql}(\omega)$ provides an identically zero real part. The quasi-elastic contribution in the neutron spectra was modelled by a $\delta$-function as the expected maximum FWHM of the line is $\simeq$ 0.2 meV FWHM based on the experimental value of the self-diffusion coefficient [166,167]. Also, an elastic contribution was used to fit the central part of the coherent x-ray $S^{\exp}(q,\omega)$. The fit was performed by assuming $U_{ll} = 0$, as this constant can be embodied into $\omega_{ql}^2$, and $U_{12}(q) = q\,U_0 \exp(-\lambda q)$. Over the present limited $q$ range, the fit was found not to depend on the value of the decay constant

$\lambda$, while the linear dependence of $U_{12}(q)$ al low $q$ guaranteed the existence of an acoustic mode.

This model provided a good and stable fit of all the available common data from the neutron and x-ray experiments over the wavevector transfer range 0.3 $\text{Å}^{-1}$ to 1.2 $\text{Å}^{-1}$. The results of the fit with the best-fitting curve resulting from the superposition of the two interacting modes $l = 1, 2$, are shown in Figure 9 in comparison with the experimental spectra of neutrons, panel $(a)$, and x-rays, panel $(b)$. Neutron data are presented on log scale because of the quasi-elastic incoherent contribution much higher than the inelastic coherent part of the cross-section. The latter term is proportional to the low value taken by the static structure factor at low momentum, namely $S(q) \simeq 0.02$. Looking at the figures it is evident that the model fits correctly also minute details of the dynamic structure factors of both experiments at all momentum values.

In panel $(a)$ of Figure 9, an enlarged view of a portion of the spectrum is also presented to show the specific peculiarity of the model. In the present description, the $S_{11}(q, \omega)$ structure factor contains a sort of double-peak structure in the region where the interaction is more active, that is in the region where $\omega_{q1}$ and $\omega_{q2}$ are close to each other. In addition, the shape of $S_{ll}(q, \omega)$ is not similar to the sum of two DHO functions, an approximation which has been applied in several analyses reported in past literature [74,75]. We remark that the interaction model is more general than the scheme with the sum of different DHOs functions, which is actually recovered in the limit of low interaction. The interaction model facilitates a correct physical interpretation of the data. Indeed, in the ideal case of a homogeneous isotropic continuum, two modes, a longitudinal and a transverse one, are expected, although only the longitudinal mode can contribute to the scattering, as the transverse mode does not affect the system density-density correlation. In the present model, the interaction can transfer part of the transverse oscillator strength from the transverse to the longitudinal mode so that the visibility of both modes is possible in the neutron and x-ray inelastic scattering experiments.

Using the results of the present fit, the *bare* dispersion relations of the two modes were obtained together with the integrated intensities which provide a measure of the strength of the individual modes. A transverse character can be attributed to the observed low-intensity modes even though in complex samples, like molecular ones, also longitudinal optic modes, with negligible strength, can be present. The dispersion relations and the integrated intensities are shown in Figures 10 and 11 respectively, where the negligible intensity of the mode identified as ”2” is apparent at low $q$. From the dispersion relation of the mode identified as ”1” we first confirm the previous finding on the value of the longitudinal collective-mode velocity,

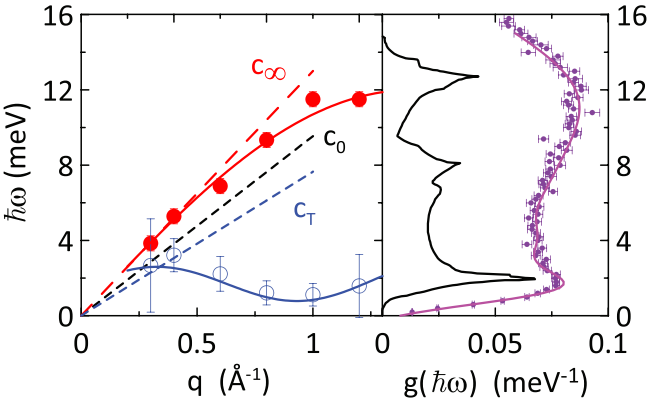


**Figure 10.** Dispersion relations of mode "1" (red dots) and mode "2" (blu circles) obtained by the two-interacting modes model applied to the unique set of neutron and x-ray data measured in liquid Hg. The full lines through the data are guide-to-the-eye. The ordinary sound velocity $c_0$ and the velocities associated to the longitudinal and the transverse modes are also shown by dashed lines. The right side of the figure shows the experimental density of states $g(\hbar\omega)$ of liquid mercury (dots) resulting from the incoherent neutron-scattering experiment. The purple continuous line through the dots is a guide-to-the-eye, while the black curve is the density of states obtained from the measurement of phonon dispersion relations in rhombohedral $D^5_{3d}$ $^{201}$Hg crystal [168]. Note the same energy axes for the two figures and the striking correspondence between the modes energy and the peaks in the density of states.

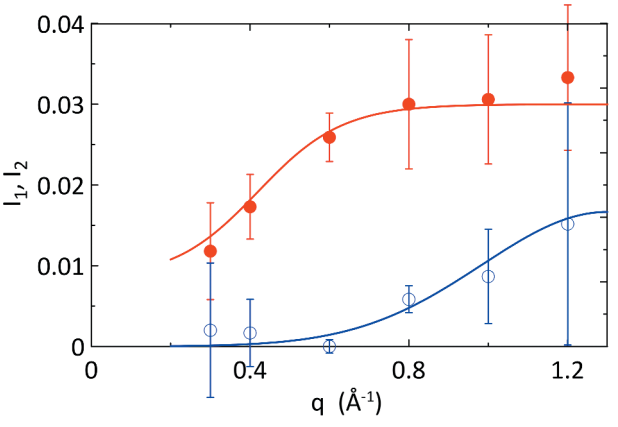


**Figure 11.** Energy-integrated intensity versus $q$ for mode "1" (red dots) and mode "2" (blu circles) obtained by the two-interacting modes model applied to the single set of neutron [159] and x-ray [160] data measured in liquid Hg. The full lines through the data are guides-to-the-eye.

that is $c_\infty = 13.0 \pm 0.5$ meV Å = 1980 $\pm$ 80 m/s, being higher than the velocity $c_0$ measured in the ultrasound region, that is $c_0 = 9.54$ meV Å = 1451 m/s. This results in a ratio $c_\infty/c_0 = 1.36 \pm 0.05$ in quantitative agreement with the previous determinations and with the results of the interacting electron gas model. The whole of these findings enables a safe identification of the mode "1" as the longitudinal acoustic one. We remark that the joint analysis of the two sets of experimental data reduces the error on the value of $c_\infty$ because of the stronger constraints resulting from fitting two sets of data with different characteristics.

As to the dispersion relation of the mode identified as "2" we observe that it extends also at low $q$ where the mode has a negligible strength, thanks, however, to the transfer effect on the mode identified as "1". The behaviour of "2" at low $q$ does not help to make a specific identification, however, applying the guess of Ref [60], the experimental difference between $c_\infty$ and $c_0$ provides ideally a transverse dispersion relation with associated velocity $c_T = 7.7 \pm 0.6$ meV Å = 1160 $\pm$ 100 m/s at low $q$. From the value of $c_T$ a linear dispersion is produced that crosses the experimental data of the mode "2" at an energy consistent with the identification of the mode as transverse acoustic.

Further information, crucial to disentangle the complex scenario of the collective-mode dispersion in Hg, is obtained using the incoherent neutron-scattering data that provides the density of states $g(\hbar\omega)$. Despite the very high absorption cross-section of about 800 b per atom at the neutron energy of the IN5 experiment (3.129 meV), it was possible to get an accurate determination of $g(\hbar\omega)$ over the energy range up to about 16 meV. Above 16 meV, the subtraction of the peak due to the inelastic scattering from the aluminium container was not possible. The experimental $g(\hbar\omega)$ is shown in Figure 10 where a quite smooth density of states is apparent, as expected for a disordered material where the dispersion relation does not exhibit critical points and the modes are strongly damped. The data show two clear maxima located at the energy values corresponding to the maximum energy of mode "1" and to the average energy of mode "2". This result, obtained from a completely different set of data and without the support of a model for $g(\hbar\omega)$ data analysis, is a very strong indication for the interpretation of the collective mode behaviour. Indeed, the structure of the density of states contains two main frequency contributions at about 1.5 meV $\simeq$ 0.36 THz, that is very close to the average frequency of the mode "2", and the other at about 11.5 meV $\simeq$ 2.78 THz.

It is also interesting to make a comparison with the phonon dispersion relations measured in Ref [168]. on the rhombohedral $D^5_{3d}$ $^{201}$ Hg crystal, with density $\rho = 14.40$ g/cm$^3$ at 80 K. The so obtained density of phonon

states is also shown in Figure 10 to facilitate the comparison with the present findings in liquid Hg. The results of the crystal experiment show the presence of two peaks in the density of phonon states located at about 2.1 meV $\simeq$ 0.51 THz and 12.7 meV $\simeq$ 3.07 THz plus a third one at about 7.9 meV $\simeq$ 1.91 THz. The first two peaks are related to the very low energy transverse acoustic mode, and to the longitudinal acoustic mode at the zone boundary. The third peak is related to the zone boundary of the second transverse mode. This comparison suggests that in the isotropic liquid, apart from the longitudinal mode, only the lowest energy mode is retained and the observed behaviour suggests a partial transverse character as the mode intensity gets very low at low $q$. Therefore, we wish to underline the importance of determining the density of states by means of an independent incoherent scattering experiment which is a valuable support to the interpretation of the collective ion dynamics and the nature of the dispersions. This approach should be extended to other systems and not confined to fortunate cases like mercury.

As a final remark, the complex dynamics of Hg close to the metal to insulator transition has also been investigated in [169,170] by x-ray scattering. It would be extremely important to carry out further neutron studies, coherent and incoherent, of this challenging topic, despite the extreme conditions of the measurements that require improved instrumentation at the new sources.

### 7.2. Gallium, the unsolved excess of signal

Gallium can be regarded as a *border line* element that is metallic in both solid and liquid state but with a low electrical and thermal conductivity. Very interestingly, it is the element with the highest ratio between boiling and melting points, namely $T_b/T_m = 8.82$. Comparing this value with that of other elements it is evident that Ga is a very special case [157]. Indeed, the ratio $T_b/T_m$ ranges from values close to 2 for elements like transition metals, while relatively high values are observed in alkali metals and heavy polyvalent metals, like Tl, Pb, Bi, and even higher values are found for In and Sn, as reported in Table 2. Also the pressure dependence of $T_m$ in Ga is rather anomalous considering that $T_m$ decreases on increasing the pressure above the ambient value up to 1 GPa [171]. This situation is not very common but it is present in some elements that in solid phase show changes of the crystal structure on increasing pressure. The origin of the very large temperature region of stability of the liquid phase in normal conditions is difficult to explain but the thermodynamic behaviour of all the materials is strictly related to the ion dynamics, and specifically to collective excitations, as this is the major contribution to the internal energy of the system.

From the experimental point of view, Ga is the fortunate case where high-temperature experiments are made easier by a low $T_m$ and a wide temperature range of liquid stability. Therefore, Ga is a well-suited simple system to test the temperature-dependent effects on the atomic THz dynamics, and to prove the validity of the interpretation by plasma based and interacting modes models. In crystals, on increasing temperature, a shortening of the phonon lifetime is expected due to the activation of anharmonic interactions. In liquids, collective modes are affected by a rather strong damping that in the hydrodynamic limit is related to longitudinal kinematic viscosity and thermal diffusivity. Considering that the simple extrapolation of the hydrodynamic result from low frequency to the THz range does not work, the high damping observed in this frequency region should be attributed to processes different from those expected for the classical fluid in the continuum limit, so that temperature-dependent investigations represent a fundamental source of information.

In previous neutron and x-ray scattering investigations [172–176], a relatively simple picture of Ga collective modes emerged with a propagation velocity of about 20 meV Å $\simeq$ 3100 m/s, a value about 10% higher than the sound velocity measured in the ultrasound regime [177]. This data is lower than the value 25.79 meV Å $\simeq$ 3921 m/s provided by electron gas-based calculations with the exact local-field correction [89], which, contrary to Hg, indicates a non-negligible ion plasma contribution. Further investigations revealed complex features [178] in the collective excitation spectra, similarly to the case of mercury, indicating deviations from the simple models with just one longitudinal acoustic mode. These deviations, though apparently quantitatively small, are nonetheless the fingerprints of the complex nature of the interactions, which require more sophisticated models to describe the experimental data. Gallium, like mercury but without sharing with it a large incoherent cross-section [4], shows an excess of quasi-elastic scattering [179]. Various investigations of this effect have been unable to establish the origin of the excess of scattering after having excluded even effects originating from possible magnetic contributions [165,104].

Here, we concentrate on the inelastic collective dynamics as the available experimental data can be used for a more detailed analysis allowing to draw a picture of Ga close to that of Hg. Overall considering that the incoherent scattering in gallium is low in absolute terms, as clearly supported by the direct comparison of INS and IXS data in Ref [174]., we present a new analysis based on the model with two interacting modes for the data of Ref [174]. where $S^{\mathrm{exp}}(q,\omega)$ is measured at two different temperatures from $q =$ 1 Å$^{-1}$ down to $q =$ 0.25 Å$^{-1}$, a value low enough to appreciate the effect of the mode–mode interaction on the collective-mode velocity. The lowest

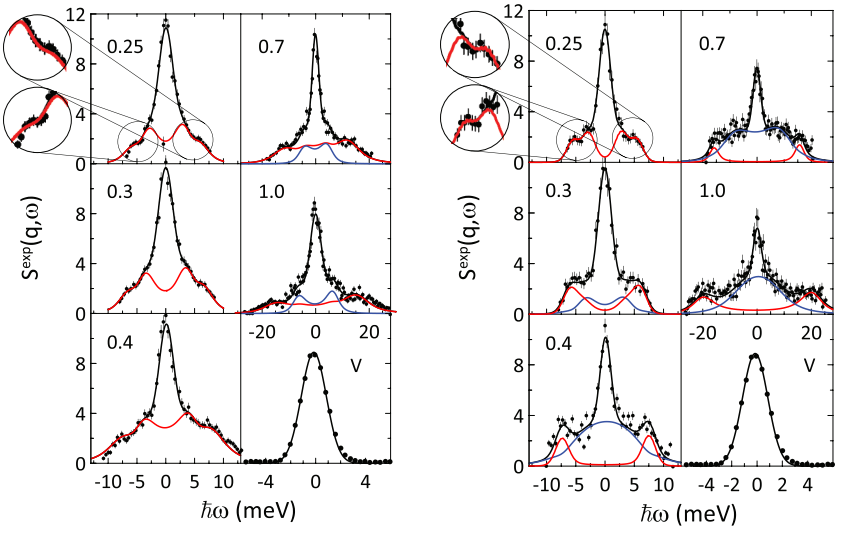


**Figure 12.** Experimental dynamic structure factor of liquid Ga versus exchanged energy, at the different values of wavevector transfers $q$ [174]. Panel (a): neutron experiment at $T = 320$ K; panel (b): neutron experiment at $T = 970$ K. The black full lines are the best-fitting curves obtained by the interacting modes model limited to 2 modes. Contribution from mode "1": red line; contribution from mode "2": blue line. The enlarged views of the spectra in the upper left panels show the ability of the model to reproduce details of the lineshape. The intensity measured in a Vanadium standard, which provides an estimate of the resolution, is also plotted.

temperature of the experiment was 320 K, close to the melting point, while the highest temperature was 970 K, 3.2 times the melting temperature. We, therefore, expect that over this temperature variation range, temperature-dependent effects should appear.

The previous analysis of the spectra was based on a single DHO plus a quasi-elastic peak and the finding was found that the temperature increase produced a minor effect only. However, it is important to note that, although the single-mode model is statistically adequate, the raw data contain indication of more complex features existing, as also suggested by the more recent neutron-scattering experiment of Ref [178].

The interacting model limited to two modes fits the experimental data at both temperatures, and the quality of the results is evident from Figure 12 where the experimental dynamic structure factor and the best-fitting functions are shown. As in the case of mercury, the presence of the interaction produces a visible change of the two inelastic components of the model with respect to the shape expected for the DHO function. Although the fit is of the same quality at the two temperatures, a change in the shape of the two modes is apparent at the two temperatures. The resulting dispersion relations $\hbar\omega_l(q)$ are plotted in Figure 13 that shows a limited temperature effect, as qualitatively suggested by the plot of the dynamic structure factors $S_{ll}(q,\omega)$.

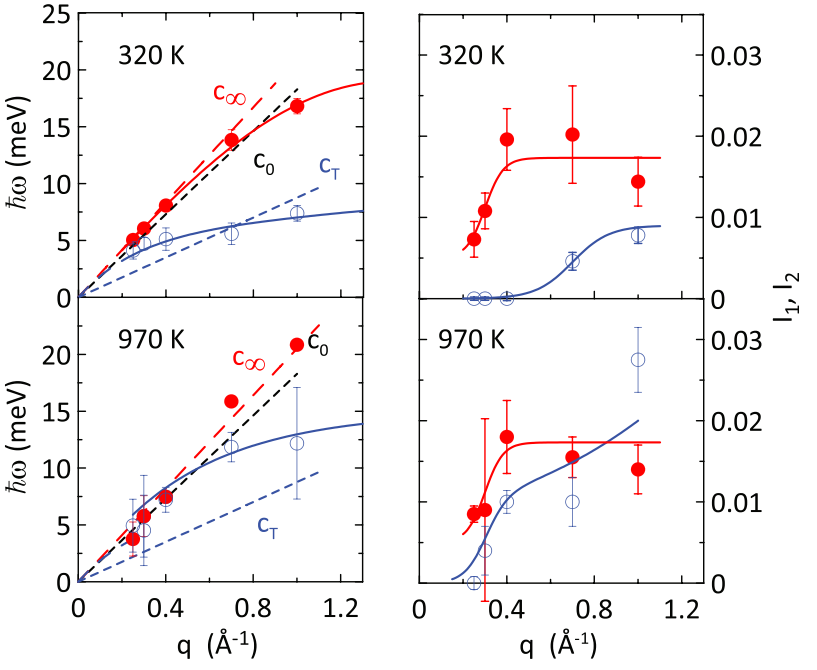


**Figure 13.** Dispersion relations of mode ″1″ (red dots) and mode ″2″ (blue circles) obtained by the two-interacting modes model applied to the neutron data measured in liquid Ga [174] at $T = 320$ K (upper left panel) and $T = 970$ K (lower left panel). The full lines through the data are guides-to-the-eye. The ordinary sound velocity $c_0$ and the velocities associated to the longitudinal and the transverse modes are also shown by dashed lines at the two temperatures. On the right-hand side of the figure, the energy-integrated intensities versus $q$ for mode ″1″ (red dots) and mode ″2″ (blue circles) are plotted at the two temperatures. Full lines through the data are guides-to-the-eye.

However, it is interesting to observe that, first, the energy of the mode ”2” tends to increase from an average value of about 6 meV to something like 10 meV and, second, the sound velocity measured at 31 MHz [180] decreases from 2878 m/s = 18.9 meV Å, at 320 K, down to about 2680 m/s = 17.6 meV Å, at 970 K. The decrease of $c_0$ is paralleled by an almost constant value of $c_\infty$ equal to 20.5 $\pm$ 1.5 meV Å = 3120 $\pm$ 200 m/s, so that $c_\infty/c_0$ increases from 1.085 $\pm$ 0.080 at $T = 320$ K to 1.18 $\pm$ 0.08 at $T = 970$K. This finding indicates that in the THz range the elastic properties of the liquid reflect a system compressibility at high frequency decreasing slower than at low frequency, as expected in a model where the liquid behaviour at high frequency resembles more closely a solid. As a consequence, using the definition of eq. (6) for the *transverse* sound velocity we get $c_T \simeq$ 6.9 meV Å $\simeq$ 1050 m/s at 320 K and $c_T \simeq$ 9.7 meV Å $\simeq$ 1500 m/s at 970 K in agreement with the suggestion that, on increasing temperature, liquid Ga takes on more solid-like characteristics.

The integrated intensities of the dynamic structure factors $S_{ll}(q,\omega)$ were calculated as a function of $q$ and removing the Bose population factor, to obtain the mode strengths at the two temperatures. The results are presented in Figure 13 where it is apparent that at $T = 320$ K the behavior of Ga is very similar to that observed in mercury, namely the behaviour of the mode identified as "1" corresponds to a longitudinal acoustic excitation with a finite intensity at low momentum, whereas the excitation "2" shows a negligible intensity, which becomes appreciable only at $q \geq 0.7$ Å$^{-1}$. Nonetheless, the existence of mode "2" at low $q$ is evident as the interaction deforms the response of the mode "1". At $T = 970$ K the contribution of mode "2" increases with respect to $T = 320$ K, while the longitudinal acoustic mode "1" behaves similarly at both temperatures. We note that the different behaviour of $S_{22}(q,\omega)$ is directly visible in Figure 12 already at $q = 0.3$ Å$^{-1}$.

The overall trend observed by modelling the experimental data with more than one mode and introducing the mode interaction suggests that this is an effective approach to disentangle the different contributions to the liquid dynamics, consistently with the physics of neutron and x-ray scattering. From these results, it is evident that within this framework, the presence of minor details as those apparent in the magnified particulars of Figure 9 and Figure 12 can be emphasized.

### 7.3. Lithium-ammonia solutions and low momentum collective modes

The lithium-ammonia solutions, as well as the ammonia solutions of the other alkali metals, are extremely interesting and extensively studied systems with a rich phase diagram also characterized by non-metal to metal transitions. When in solution, as an effect of the solvation of the metal ions, the outermost electrons of the alkali metal are released in the liquid and the solution in metal phase can be depicted as solvated ions immersed in the free conduction electron gas. In the specific case of lithium-ammonia solutions, the electron densities associated to the metallic phase are very low [181], and the parameter $r_s$ can be adjusted to values between 7.4 and 11.3, which are substantially lower than a typical liquid metal. This is a very unique opportunity to test the stability of the electron gas beyond the limit of the ordinary metallic density range and, by a proper choice of the Li concentration and the thermodynamic conditions, an electron gas density two times smaller than Cs, that is the lowest electron density stable system, can be obtained. In addition, the phase diagram of lithium-ammonia solutions presents a possible Mott non-metal to metal transition [182,183] on lowering the temperature.

The unique features of the alkali-ammonia solutions stimulated several studies aiming to describe the actual electron distribution by means of simulation techniques [184–190]. The electron distribution was found to depend on the composition of the solution, being, for the saturated solution, very well approximated by the simple model of a homogeneous low-density electron gas. It is worth to note that over the whole concentration range, the electron density is always lower than the critical density value corresponding to a negative screening parameter $k_s^2$, which implies the instability of the electron gas. On the contrary, the system is stable and this is related to the ion–ion interactions and the ion size.

In the last two decades, several investigations by both neutron and x-ray elastic and inelastic scattering have been performed to characterize the structure [191–194] and to analyse the ion dynamics of lithium-ammonia solutions with special emphasis on the relationship with the electron distribution [195–199]. These studies revealed that very well-defined collective modes exist up to $q \leq 0.6$ Å$^{-1}$ with a dispersion relation typical of a longitudinal mode and an associated velocity $c_\infty$ obtained from the neutron data about 20% higher than the sound velocity $c_0$ measured in the MHz range. The composition dependence of the fast sound velocity shows the same trend as $c_0$ and can be interpreted by resorting to the simple Bohm-Staver approximation. More interestingly, an anomaly of the dispersion relation in saturated lithium-ammonia solution, 20 mole% metal, mpm, Li $(NH_3)_4$, is observed at $q \simeq 0.8$ Å$^{-1}$, a value fairly close to twice the Fermi momentum associated to $r_s \simeq 7.4$ for this system ($k_F = 1/(\alpha r_s) \simeq 1.9192/r_s$ a.u. = 0.2594 = 0.4901 Å$^{-1}$). The anomaly actually consists of a sudden decrease of the mode energy $\hbar\omega(q)$ which appears to be localized [195,196,198,199] over the range 0.8 Å$^{-1}$-1 Å$^{-1}$. The anomaly seems to weaken on reducing the Li content without any visible change of position. Various conjectures have been formulated to explain the anomaly at about $2k_F$, among which the Kohn anomaly. A satisfactory explanation is still lacking.

Understanding the role of the electron gas on the vibrational dynamics of a system as complex as $Li(NH_3)_4$ requires at least the knowledge of the average conduction electron density. As simple as it might appear, this is not a straightforward data as the simple assumption of one electron from Li being distributed over the whole system volume is not supported by experimental evidence. In [89], the key guess was that the average *interstitial* electron density is the electron parameter driving the ion screened response, and a rather sophisticated protocol requiring the knowledge of the average structure of the system was proposed to determine the density in pure liquid metals. The application of that approach to obtain the lithium-ammonia relevant density, although feasible, is made complex by the non-elemental

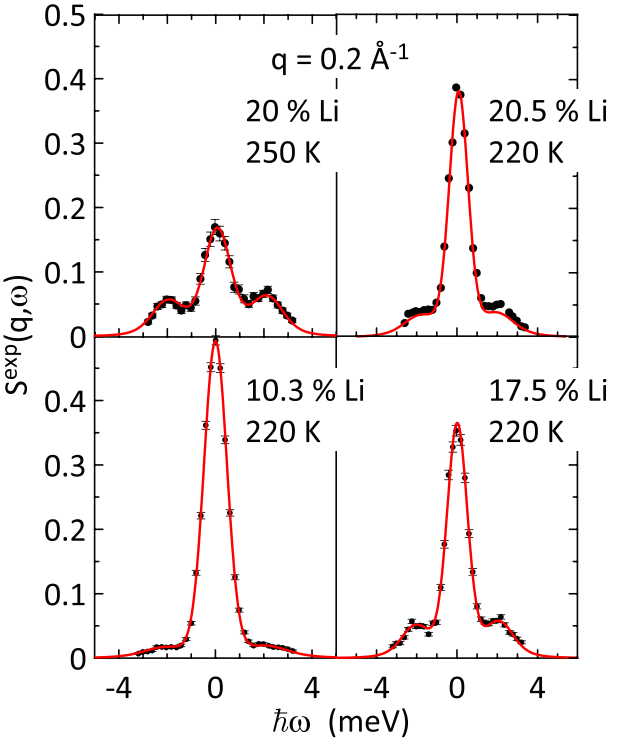


**Figure 14.** Experimental dynamic structure factor of lithium-ammonia solutions at different metal concentration. The data are shown at the minimum value of measured wavevector transfer $q$ =0.2 Å$^{-1}$.

**Table 3.** Collective-mode velocity of lithium-ammonia solutions derived by neutron and x-ray experiments. The first column reports the experimental probe and the reference work. $c_0$ is the ordinary sound velocity. $c_\infty$ is obtained by the $q \to 0$ linear extrapolation of the dispersion relation obtained by a DHO fitting of the dynamic structure factor. The values of electron gas parameter $r_s$ are calculated under the simplifying assumption $Z_{Li} = 1$. $c^a_{BS}$ and $c^b_{BS}$ are the velocities calculated using the Bohm-Staver model with two approximations for the ion plasma frequency (see text).

| Probe | Li% | $T$ (K) | $c_0$ (meV Å) | $c_\infty$ (meV Å) | $r_s$ | $c^a_{BS}$ (meV Å) | $c^b_{BS}$ (meV Å) |
|---|---|---|---|---|---|---|---|
| n [200] | 10.3 | 220 | 9.58 | 12.6 ± 0.7 | 8.95 | 10.29 | 8.10 |
| n [200] | 17.6 | 220 | 9.51 | 11.4 ± 0.7 | 7.64 | 12.63 | 9.49 |
| n [199] | 20.5 | 220 | 9.48 | 11.4 ± 0.7 | 7.38 | 13.31 | 9.82 |
| n [198] | 20.0 | 250 | 9.40 | 11.0 ± 0.2 | 7.42 | 13.20 | 9.77 |
| x [196] | 13 | 240 | 9.53 ± 0.13 | 10.2 ± 0.5 | | | |
| x [196] | 16 | 240 | 9.53 ± 0.16 | 9.7 ± 0.5 | | | |
| x [196] | 20 | 240 | 9.60 ± 0.10 | 10.1 ± 0.7 | | | |

nature of the system and its microscopic structure. Data on the electron density in lithium-ammonia could also be obtained by the plasmon dispersion measured in the x-ray scattering experiment of [195] over the eV energy range, that is well above the typical collective-mode energy.

However, such an approach would require a complex and consistent analysis of the dielectric function over the meV and the eV energy ranges, for which further experimental data and theoretical models are needed.

Here, we focus the analysis on the low wavevector data of the dynamic structure factor available from x-ray [196,197] and neutron [198,199] experiments, including new unpublished neutron data [200] collected on a 17.5% Li sample at $T = 220$K. The purpose is to examine the slow to fast sound transition in lithium-ammonia solutions and to deduce the $c_\infty$ velocity from the $q \to 0$ extrapolation of the dispersion curves.

Typical neutron spectra collected for different Li concentrations in fully deuterated solutions [198–200] are shown in Figure 14 at the lowest wavevector transfer $q$=0.2 Å$^{-1}$. A well-defined collective mode is observed in the spectra, despite the non-negligible incoherent contribution due to the large number of deuterium atoms in the samples. In Figure 14, the best-fitting curves produced using a single DHO function to model the inelastic components of the experimental dynamic structure factor are also shown. An additional analysis based on the interacting modes model, was carried out and found to provide an excellent fit of the data with an interpretation scheme for the vibrational spectra of lithium-ammonia solutions. The full description of this approach is given in a forthcoming, specialized publication [200].

Table 3 summarizes the results on the THz collective-mode velocity obtained analysing both neutron and x-rays data in diverse Li concentrated solutions at close temperatures. Specifically, the values of $c_\infty$ are determined from the DHO fitting of the spectra, while the Bohm-Staver predictions are obtained using both the inverse of the average mass (column 7 of Table 3) and the average of the inverse mass [64] (column 8 of Table 3) to calculate the ion plasma frequency, that is

$$\Omega_p^2 = 4\pi n_i (Z_i e)^2 \frac{1}{\langle M \rangle} \quad \text{and} \quad \Omega_p^2 = 4\pi n_i (Z_i e)^2 \langle \frac{1}{M} \rangle$$

A first inspection of Table 3 shows systematic trends, namely the neutron obtained $c_\infty$ is higher than both $c_0$ [201] and $c_\infty$ from x-rays. The latter effect can be explained by the different coupling of the two probes. Indeed, while neutrons interact more with the light deuterium atoms, which represent 66% of the total cross-section, the x-ray photons couple to the nitrogen atoms that represent 93% of the total cross-section at $q = 0$. This percentage increases on increasing the wavevector due to the faster lithium and hydrogen form factors decrease. Therefore, the higher $c_\infty$ seen by neutrons is not related to the mass difference between hydrogen and deuterium, as that would produce the reverse effect being the deuterated sample 16% heavier than the hydrogenated one. The observed effect is probably produced by the

faster dynamics explored by neutrons that couple to deuterium atoms while photons probe the slower dynamics of the heavier nitrogen atoms.

The data show an increase on decreasing the Li concentration, as also observed by the measurements in the MHz range [201]. Further, the velocities resulting from the Bohm-Staver approximation with $r_s = aZ_{Li}^{1/3}$ and $Z_{Li} = 1$, independently of the mass average, show a wrong increasing trend with increasing the Li concentration, contrary to the experimental findings at both the MHz and THz frequency regions. The Bohm-Staver approximation produces a correct order of magnitude of the mode velocity, which can be taken as an indication of the relevant role played by the electron density, although this simple model, failing to reproduce trends, should be left behind in favour of more complex schemes.

In conclusion, although the lithium-ammonia solutions have been the subject of several studies, a coherent description is not yet available. Considering the results of molecular dynamics simulation [190] and the newly reported complexity of this system [181], more extended investigations, including purely incoherent neutron-scattering experiments with polarisation analysis option to determine the density of states, should be carried out.

## 8. Conclusions and outlook

Nowadays, liquid metals are receiving great attention as advanced functional materials for novel applications that exploit the material flexibility coupled to the high electrical conductivity. Indeed, current technologies enable to transform the potential contained in these material characteristics into effective applications, notably *transient devices, soft robotics, biomedical sensing, and health monitoring* according to [202]. The impact of Hg and Ga as adaptative sensors [203] and Ga-based alloys as biomaterials [204] is actively investigated. Parallel to these application-oriented studies, understanding fundamental physical mechanisms of the liquid metal behaviour continues to be an active field of both theoretical and experimental research [181].

The knowledge of the ion dynamics is key to the statistical thermodynamics interpretation of liquid systems, with specific heat providing a paradigmatic example [205] and traditional computational approaches, like first principle molecular dynamics simulations, although limited to relatively reduced number of atoms and rather short time scales, provide an accurate description of the vibrational properties. Yet, continuous development of interpretation schemes, even if not a holistic theory of the complex liquid system, is of great importance to frame the experimental results. On the other hand, x-rays and neutron inelastic scattering

experiments represent unrivalled tools for the investigation of the microscopic dynamics of liquids, and liquid metals, over the THz region.

The potential of the x-ray technique has been fully deployed over the last twenty years and enabled reaching unprecedented experimental insight in the liquid vibrational dynamics. Neutron techniques offer a major perspective for the coming years if the increase of intensity effectively available at the sample, as expected from the new high-intensity sources operation, will allow to significantly improve the energy and momentum resolution. An example of how important is the instrument **resolution**, not at the price of an intensity loss, is given by the analysis here presented of the Hg and Ga dynamic structure factor where the interacting mode model facilitates the interpretation of experimental spectra pointing out at relatively tiny ill-resolved structures that support the existence of *transverse* excitations at THz frequency. The complexity of the dynamic response in liquid metals, as well as in companion disordered systems like glasses and biological samples, could be more easily interpreted, and the nature of the propagating excitations, better understood by high-resolution measurements at the new instruments.

Increased neutron instrument performances in terms of available **intensity**, on the other hand, represent a real opportunity for the investigation of the dynamic response in samples of reduced size. The best example is given by biomaterials like proteins or membranes where sample deuteration is critical to distinguish and identify the dynamics of the hydrogen-rich segments. Despite the recent developments, deuteration remains a complex technique and the production of large sample quantities is still cost- and time-limited [206]. An estimate of the order of magnitude can be obtained by inelastic scattering experiments carried out on biological samples, like the dry maltose binding protein [207] where quantities of deuterated sample as large as 0.5 g were needed for a complete analysis of the dry protein dynamics. Actually, as discussed in [207], a considerable fast sound effect was observed ($c_\infty = 3780 \pm 130$ m/s at 2 THz versus an ordinary sound velocity $c_0 = 2000 \pm 30$ m/s at 2 MHz) together with a second collective mode at 5 meV $\simeq$ 1.21 THz resembling a similar excitation observed at 6 meV $\simeq$ 1.45 THz in water. A closer inspection of the 5 meV mode was possible thanks to incoherent neutron-scattering measurements on the hydrogenated counterpart of the dry protein, which provided the density of vibrational states of the system. This study serves as a model clearly indicating the further developments that would improve accuracy and reliability of the experiments, namely a much higher intensity and the polarisation option. A higher intensity at the sample would enable widening the set of measurements to a temperature-and hydration-dependent study, with crossing the dynamic transition at $\sim$200 K and analysing the dynamic response of the biologically active hydrated protein. Polarisation analysis

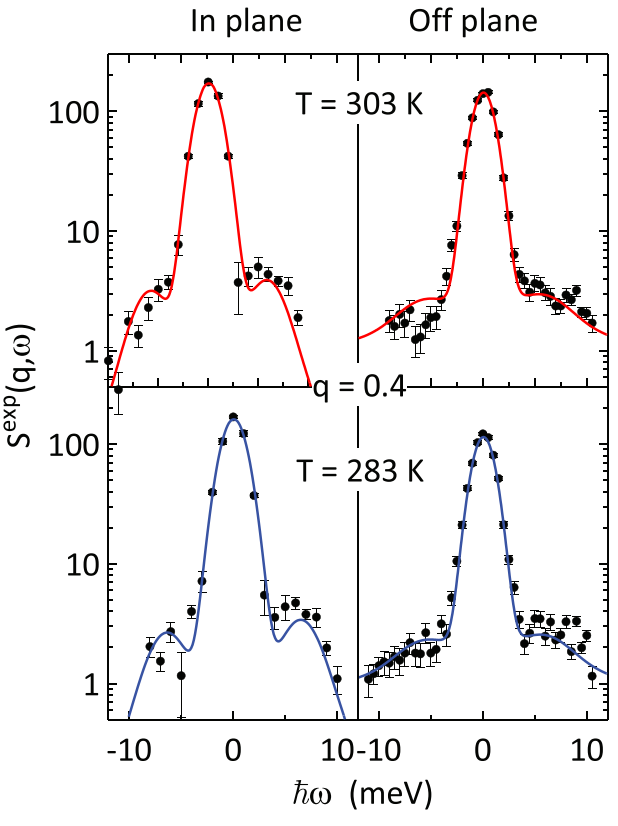


**Figure 15.** Experimental dynamic structure factor of the oriented phospholipid membrane versus exchanged energy. The data collected in the two configurations "in-plane" and "off-plane", and extracted by the PSD detector in a single measurement, are shown for the wavevector transfer $q = 0.4$ Å$^{-1}$ at the two temperatures 283 K (bottom panel) and 303 (top panel). The full lines are DHO plus central Lorentzian fitting curves.

would enable to separately measure coherent and incoherent contributions in the cross-section of deuterated and hydrogenated proteins, emphasizing the distinctive role of isotopic substitution.

The inelastic neutron technique, exploiting the time of flight configuration, offers the further advantage of exploring in one sole experiment an entire reciprocal space volume of the wavevector transfer **q** and a wide exchanged energy range, by collecting the scattered neutrons on a large area (up to more than 10 m$^2$) PSD detector, which could be beneficially applied at the instruments operated at the intense-pulsed sources. The favourable conditions of operating a large area detector are pointed out by the case study of Figure 15, where the dynamic response of an oriented phospholipid membrane is shown. A keen analysis of the data collected in one shot by the PSD 2d-detector provides the simultaneous measurement of the "off-plane" and the "in-plane" dynamic response of the two-dimensional membrane. The membrane is characterized by "in-plane" disorder and

Figure 15 shows, at a given wavevector transfer $q$, the lower signal associated to the "off-plane" dynamics. This option can be successfully exploited for the study of 2d systems, membranes and liquid-liquid interfaces, where the response along the different planes can be collected and analysed with the sample, and the whole experimental configuration, fixed.

Future intense neutron sources serving an optimized instrument park would enable studies of increased complexity on disordered and low-dimensional systems, with the characterization of the inelastic response in biomaterials, and its relationship with the material functionality, as a challenging perspective for the coming years.

## Acknowledgments

We wish to acknowledge the Institut Laue Langevin (Grenoble, France) for providing neutron beam time and for support during the experiments. The collaboration with F. Barocchi, LE. Bove, G. D'Angelo, A. De Francesco, F. Demmel, B. Dorner, F. Formisano, E. Guarini, A. Ivanov, A. Laloni, A. Orecchini, A. Paciaroni, L. Sani, J-B. Suck, and M. Zanatta is kindly acknowledged.

## Disclosure statement

No potential conflict of interest was reported by the authors.

## Funding

This work is supported by the cooperative agreement for the development of the project CarESS.

## References

[1] Lovesey SW. Theory of neutron scattering from condensed matter. Oxford (UK): Clarendon; 1987.
[2] Skold K, Price DL, editors. Methods in experimental physics; Vol. 23. Part A. London (UK): Academic Press; 1986.
[3] Windsor CG. Pulsed neutron scattering. London (UK): Taylor & Francis; 1981.
[4] Dianoux AJ, Lander G, editors. Neutron data booklet. Philadelphia (US): Old City Publishing; 2003.
[5] Cavaye CH. Neutron spectroscopy: an under-utilised tool for organic electronics research? Angew Chem Int Ed. 2019 Jul;58:9338–9346.
[6] Hippert F, Geissler E, Hodeau JL, et al., editors. Neutron and X-ray spectroscopy. The Netherlands: Springer; 2006.
[7] Liebschner D, Afonine PV, Baker ML, et al. Macromolecular structure determination using X-rays, neutrons and electrons: recent developments in Phenix. Acta Cryst. 2019;D75:861–877.

[8] Doktorova M, Kučerka N, Kinnun JJ, et al. Molecular structure of sphingomyelin in fluid phase bilayers determined by the joint analysis of small-angle neutron and X-ray scattering data. J Phys Chem B. 2020 May;124:5186–5200.
[9] Semeraro EF, Marx L, Frewein MPK, et al. Increasing complexity in small-angle X-ray and neutron scattering experiments: from biological membrane mimics to live cells. Soft Matter. Feb 2020; doi:10.1039/c9sm02352f.
[10] Weinberg AM. Oak ridge national laboratory. Science. 1949 Mar;109:245–248.
[11] Shull CG, Strauser WA, Wollan EO. Neutron diffraction by paramagnetic and antiferromagnetic substances. Phys Rev. 1951 Jul;83:333–345.
[12] Anderson PW. More and different: notes from a thoughtful curmudgeon. Singapore: World Scientific. 2011;pp. 404–408.
[13] Carlile CJ The ILL Millennium programme. Institut Laue-Langevin, Grenoble (FR): April 2001 Internal Report.
[14] Petry W. Advanced neutron instrumentation at FRM-II. Atw Internationale Zeitschrift fuer Kernenergie. 2003;48:315–318.
[15] Bennington SM, Campbell SI, Broome TA, et al. ISIS target station II: preliminary target and moderator simulations. J Neutron Res. 2003 May;11:93–98.
[16] Henderson S, Abraham W, Aleksandrov A, et al. The spallation neutron source accelerator system design. Nuc Inst Methods Phys Res Sec A. 2014 Jun;763:610–763.
[17] Carlile CJ, Petrillo C. editors.Neutron scattering facilities in Europe present status and future perspectives. Vol. 1. ESFRI Scripta Universitá degli Studi di Milano (IT): September 2016.
[18] Peggs S, editor, ESS technical design report, April 2013. doi:10.13140/RG.2.1.2040.6483/1
[19] Mezei MF. The raison d'être of long pulse spallation sources. J Neutron Res. 1997;6:3–32.
[20] Zanini L, Andersen KH, Batkov K, et al. Design of the cold and thermal neutron moderators for the European spallation source. Nucl Instrum Methods Phys Res A. 2019;925:33–52.
[21] Andersen KH, Argyriou DN, Jackson AJ, et al. The instrument suite of the European spallation source. Nuc Inst Methods Phys Res Sec A. 2020;957:163402.
[22] Blume M. Polarization effects in the magnetic elastic scattering of slow neutrons. Phys Rev. 1963 Jun;130:1670–1676.
[23] Maleev SV, Bar'yakhtar VG, Suris RA. Fiz. Tverd Tela (Leningrad). 1962;4:3461.
[24] Blume M. Neutron polarization phenomena in scattering processes. Physica B. 1999;**267- 268**:211–214.
[25] Moon RM, Riste T, Koehler WC. Polarization analysis of Thermal-Neutron Scattering. Phys Rev. 1969 May;181:920–931.
[26] Halpern O, Johnson MH. On the magnetic scattering of neutrons. Phys Rev. 1939 May;55:898–923.
[27] Hicks TJ. Experiments with neutron polarization analysis. Adv Phys. 1996 Nov;45:243–298.
[28] Chatterji T, editor. Neutron scattering from magnetic materials. Amsterdam (NL): Elsevier B.V; 2006.
[29] Chisnell R, Helton JS, Freedman DE, et al. Topological magnon bands in a kagome lattice ferromagnet. Phys Rev Lett. 2015 Sep;115:147201.
[30] Soh J-R, de Juan F, Qureshi N, et al. Ground-state magnetic structure of $Mn_3Ge$. Phys Rev B. 2020 Apr;101:140411(R).

[31] Brown PJ, Nunez V, Tasset F, et al. Determination of the magnetic structure of $Mn_3Sn$ using generalized neutron polarization analysis. J Phys Condens Matter. 1990 Aug;2:9409–9422.
[32] Leliévre-Berna E, Bourgeat-Lami E, Fouilloux P, et al. Advances in spherical neutron polarimetry with Cryopad. Physica B: Condens Matter. 2005;356:131–135.
[33] Di Fabrizio E, Mazzone G, Petrillo C, et al. Spin-density of ordered FeCo - A failure of the local-spin-density approximation. Phys Rev B. 1989 Nov;40:9502–9507.
[34] Dalla Piazza B, Mourigal M, Christensen NB, et al. Fractional excitations in the square-lattice quantum antiferromagnet. Nat Phys. 2015 Jan;11:62–68.
[35] Arbe A, Malo de Molina P, Alvarez F, et al. Dielectric susceptibility of liquid water: microscopic insights from coherent and incoherent neutron scattering. Phys Rev Lett. 2016 Oct;117:185501.
[36] Arbe A, Nilsen GJ, Stewart JR, et al. Coherent structural relaxation of water from meso- to intermolecular scales measured using neutron spectroscopy with polarization analysis. Phys Rev Research. 2020 Apr;2:022015(R).
[37] Burankova T, Hempelmann R, Wildes A, et al. Collective ion diffusion and localized single particle dynamics in pyridinium-based ionic liquids. J Phys Chem B. 2014 Nov;118:14452–14460.
[38] Cassella G, Stewart JR, Paternó GM, et al. Polarization analysis on the LET cold neutron spectrometer using a $^3$He spin-fllter: flrst results. J Phys. 2019;1316:012007.
[39] Landau LD, Lifshitz EM. Statistical physics. Amsterdam (NL): Elsevier Ltd; 1980.
[40] Boon JP, Yip S. Molecular hydrodynamics. New York (US): McGraw-Hill; 1980.
[41] Hansen J-P , McDonald I. Theory of Simple Liquids. New York (US): Academic; 1986.
[42] March N, Tosi M. Atomic dynamics in liquids. New York (US): Dover; 1991.
[43] Ziman J. Models of disorder. Cambridge (UK): Cambridge University Press; 1979.
[44] Barker JA, Henderson D. What is "liquid"? Understanding the states of matter. Rev Mod Phys. 1976 Oct;48:587–671.
[45] Egelstaff P. An introduction to the liquid state. New York (US): Academic; 1967.
[46] Balucani U, Zoppi M. Dynamics of the liquid state. Oxford (UK): Clarendon; 1983.
[47] Allen MP, Tildesley DJ. Computer simulation of liquids. New York (US): Oxford University Press; 2017.
[48] Montfrooij W, de Schepper I. Excitations in simple liquids, liquid metals and superfluids. New York (US): Oxford University Press; 2010.
[49] Cunsolo A. The THz dynamics of liquids probed by inelastic X-ray scattering. Singapore: World Scientific; 2020.
[50] Bulavin L, Lebovka N, editors, Physics of liquid matter: modern problems. Proceedings, Kyiv, Ukraine, 23–27 May 2014. Springer Proceedings in Physics. Volume 171. Switzerland (CH): Springer International Publishing 2015.
[51] Copley JRD, Lovesey SW. The dynamic properties of monatomic liquids. Rep Prog Phys. 1975 Apr;38:461–563.
[52] Scopigno T, Ruocco G, Sette F. Microscopic dynamics in liquid metals: the experimental point of view. Rev Mod Physics. 2005 Jul;77:881–933.
[53] Pilgrim W-C, Morkel Chr. State dependent particle dynamics in liquid alkali metals. J Phys Condens Matter. 2006 Aug;18:R585–R633.
[54] Takeno S, Goda MA. A theory of phonons in amorphous solids and its implications to collective motion in simple liquids. Prog Theoretical Phys. 1971 Feb;45:331–352.
[55] Hubbard J, Beeby JL. Collective motion in liquids. J Phys C. 1969 Mar;2:556–571.
[56] Yoshida F, Takeno TS. Dynamical correlations and collective excitations in liquids. Phys Rep. 1989;173:301–379.

[57] Schirmacher W, Schmid B, Sinn H. Theory of collective excitations in simple liquids. Eur Phys J Special Topics. 2011 May;196:3–13.
[58] Trachenko K, Brazhkin VV. Duality of liquids. Sci Rep. 2013 Jul;3:2188.
[59] Bolmatov D, Musaev ET, Trachenko K. Symmetry breaking gives rise to energy spectra of three states of matter. Sci Rep. 2013 Sep;3:2794.
[60] Trachenko K, Brazhkin VV. Collective modes and thermodynamics of the liquid state. Rep Prog Phys. 2016 Jan; 79:3016502.
[61] Trachenko K. Lagrangian formulation and symmetrical description of liquid dynamics. Phys Rev E. 2017 Dec;96:062134.
[62] Baggioli M, Vasin M, Brazhkin V, et al. Gapped momentum states. Phys Rep. 2020 Apr;865:1–44.
[63] Copley JRD, Rowe JM. Short-wavelength collective excitations in liquid rubidium observed by coherent neutron scattering. Phys Rev Lett. 1974 Jan;32:49–52.
[64] Bove LE, Sacchetti F, Petrillo C, et al. Neutron investigation of collective excitations in liquid K-Cs alloys: the role of the electron density. Phys Rev Lett. 2000 Dec;85:5352–5355.
[65] Sinn H, Sette F, Bergmann U, et al. Coherent dynamic structure factor of liquid lithium by inelastic X-Ray scattering. Phys Rev Lett. 1997 Mar;78:1715–1718.
[66] de Schepper IM, Verkerk P, van Well AA, et al. Short-wavelength sound modes in liquid argon. Phys Rev Lett. 1983 Mar;50:974–977.
[67] Cunsolo A, Pratesi G, Verbeni R, et al. Microscopic relaxation in supercritical and liquid neon. J Chem Phys. 2001 Feb;114:2259–2267.
[68] Demmel F, Hosokawa S, Lorenzen M, et al. Propagating particle density fluctuations in molten NaCl. Phys Rev B. 2004 Jan;69:012203.
[69] Giura P, Angelini R, Datchi F, et al. High frequency dynamics and structural relaxation process in liquid ammonia. J Chem Phys. 2007 Aug;127:084508.
[70] Monaco G, Masciovecchio C, Ruocco G, et al. Determination of the infinite frequency sound velocity in the glass formero-terphenyl.. Phys Rev Lett. 1998 Mar;80:2161–2164.
[71] Orecchini A, Paciaroni A, De Francesco A, et al. Collective dynamics of protein hydration water by brillouin neutron spectroscopy. J Am Chem Soc. 2009 Apr;131:4664–4669.
[72] Teixeira J, Bellissent-Funel MC, Chen SH, et al. Observation of new short-wavelength collective excitations in heavy water by coherent inelastic neutron scattering. Physical Review Letters. 1985 Jun;54:2681–2683.
[73] Sette F, Ruocco G, Krisch M, et al. Collective dynamics in water by high energy resolution inelastic X-Ray scattering. Physical Review Letters. 1995 Jul;75:850–853.
[74] Petrillo C, Sacchetti F, Dorner B, et al. High-resolution neutron scattering measurement of the dynamic structure factor of heavy water. Physical Review E. 2000 Sep;62:3611–3618.
[75] Sacchetti F, Suck J-B, Petrillo C, et al. Brillouin neutron scattering in heavy water: evidence for two-mode collective dynamics. Physical Review E. 2004 Jun;69:061203.
[76] Cunsolo A, Kodituwakku CN, Bencivenga F, et al. Transverse dynamics of water across the melting point: A parallel neutron and X-ray inelastic scattering study. Physical Review B. 2012 May;85:174305.
[77] Pontecorvo E, Krisch M, Cunsolo A, et al. High-frequency longitudinal and transverse dynamics in water. Physical Review E. 2005 Jan;71:011501.
[78] Giordano VM, Monaco G. Fingerprints of order and disorder on the high-frequency dynamics of liquids. PNAS. 2010 Dec;107:21985–21989.

[79] Hosokawa S, Inui M, Kajihara Y, et al. Transverse acoustic excitations in liquid Ga. Phys Rev Lett. 2009 Mar;102:105502.
[80] Hosokawa S, Inui M, Kajihara Y, et al. Transverse excitations in liquid Fe, Cu and Zn. J Phys. 2015 Apr;27:194104.
[81] Zanatta M, Sacchetti F, Guarini E, et al. Collective Ion dynamics in liquid zinc: evidence for complex dynamics in a non-free-electron liquid metal. Phys Rev Lett. 2015 May;114:187801.
[82] Hosokawa S, Munejiri S, Inui M, et al. Transverse excitations in liquid Sn. J Phys. 2013 Feb;25:112101.
[83] Brockhouse BN, Pope NK. Time-dependent pair correlations in liquid lead. Phys Rev Lett. 1959 Sep;3:259–262.
[84] Brockhouse BN. Bull. Am Phys Soc Ser. II 1958;3:233.
[85] Rahman A. Propagation of Density Fluctuations in Liquid Rubidium: A Molecular-Dynamics Study. Phys Rev Lett. 1974 Jan;32:52–54.
[86] Ichimaru S. Strongly coupled plasmas: high-density classical plasmas and degenerate electron liquids. Rev Mod Phys. 1982 Oct;54:1017–1059.
[87] March NH. Liquid Metals. New York (US): Cambridge University Press; 1990.
[88] Bove LE, Petrillo C, Sacchetti F. Ion density fluctuations in liquid metals: the strongly interacting ion-electron plasma. Condens Matter Phys. 2008;11:119–126.
[89] Sani L, Petrillo C, Sacchetti F. Determination of the interstitial electron density in liquid metals: basic quantity to calculate the ion collective-mode velocity and related properties. Phys Rev B. 2014 Jul;90:024207.
[90] Ashcroft NW, Stroud D. Theory of the thermodynamics of simple liquid metals. Solid State Phys. 1978;33:1–81.
[91] Pines D, Nozieres P. The theory of quantum liquids. New York (US): W. A. Benjamin, Inc; 1966.
[92] Lide DR. Boca Raton (Florida, US): CRC Press LLC 2005. J Am Chem Soc. 2005;127:4542–14542. editor CRC Handbook of Chemistry and Physics, 85th ed. .
[93] Daeneke T, Khoshmanesh K, Mahmood N, et al. Liquid metals: fundamentals and applications in chemistry. Chem Soc Rev. 2018 Jan;47:4073–4111.
[94] Chen S, Wang H-Z, Sun X-Y, et al. Generalized way to make temperature tunable conductor–insulator transition liquid metal composites in a diverse range. Mater Horiz. 2019 Jun;6:1854–1861.
[95] Guyue B, Ren L, Xun X et al. Recent Progress on Liquid Metals and Their Applications. Adv Phys X. 2018 Mar;3:412–442.
[96] Chen S, Wang H-Z, Zhao R-Q, et al. Liquid metal composites. Matter. 2020 Jun;2:1446–1480.
[97] Van Hove L. Correlations in space and time and born approximation scattering in systems of interacting particles. Phys Rev. 1954 Jul;95:249–262.
[98] Mori H. Transport, collective motion, and brownian motion. Prog Theoretical Phys. 1965 Mar;33:423–455.
[99] Mori H. A continued-fraction representation of the time-correlation functions. Prog Theoretical Phys. 1965 Sep;34:399–416.
[100] Qureshi N, Ressouche E, Mukhin A, et al. Proof of the elusive high-temperature incommensurate phase in CuO by spherical neutron polarimetry. Sci Adv. 2020 Feb;6:eaay7661.
[101] Lovesey SW, Chatterji T, Stunault A, et al. Direct observation of anapoles by neutron diffraction. Phys Rev Lett. 2019 Feb;122:047203.
[102] Nambu Y, Barker J, Okino Y, et al. Observation of magnon polarization. Phys Rev Lett. 2020 Jul;125:027201.

[103] Steffens P, Sidis Y, Kulda J, et al. Spin fluctuations in Sr_2RuO_4 (Sr(sub2)RuO(sub4) from polarized neutron scattering: implications for superconductivity. Phys Rev Lett. 2019 Feb;122:047004.
[104] Patty M, Schoen K, Montfrooij W, et al. Polarized neutron scattering investigation of excitations at low momentum transfer in liquid Ga: the mystery continues. J Non-Crystalline Solids. 2011 Nov;357:1000–1003.
[105] Zhaoa JK, Robertson L, Herwig K, et al. Polarized neutron in structural biology – present and future outlook. Paper Presented at 9th International Workshop on Polarised Neutrons in Condensed Matter Investigations (PNCMI2012). Physics Procedia. 2013;42:39–45.
[106] Hutanu V, Luberstetter W, Bourgeat-Lami E, et al. Implementation of a new Cryopad on the diffractometer POLI at MLZ. Rev Sci Instrum. 2016 Oct;87:105108.
[107] https://europeanspallationsource.se/instruments/t-rex#science-case. Available from: https://www.fz-juelich.de/jcns/jcns-2/EN/Forschung/Instruments-for-ESS/Instruments/T-REX/artikel.html (26 Jan 2021)
[108] de Schepper IM, Cohen EGD, Bruin C, et al. Hydrodynamic time correlation functions for a Lennard-Jones fluid. Phys Rev A. 1988 Jul;38:271–287.
[109] Mryglod IM, Omelyan IP, Tokarchuk MV. Generalized collective modes for the Lennard-Jones fluid. Mol Phys. 1995 Aug;84:235–259.
[110] Bryk T, Ruocco G, Scopigno T, et al. Pressure-induced emergence of unusually high-frequency transverse excitations in a liquid alkali metal: evidence of two types of collective excitations contributing to the transverse dynamics at high pressures. J Chem Phys. 2015 Sep;143:104502.
[111] Bryk T, Wax J-F. A search for manifestation of two types of collective excitations in dynamic structure of a liquid metal: ab initio study of collective excitations in liquid Na. J Chem Phys. 2016 May;144:194501.
[112] Bryk T, Huerta A, Hordiichuk V, et al. Non-hydrodynamic transverse collective excitations in hard-sphere fluids. J Chem Phys. 2017 Aug;147:064509.
[113] Bryk T, Demchuk T, Wax J-F JN. Pressure-induced effects in the spectra of collective excitations in pure liquid metals. J Phys-Condens Matter. 2020 May;32:184002.
[114] Chushak Y, Bryk T, Baumketner A, et al. Dynamical properties of liquid binary alloys: A memory function study. Phys Chem Liq. 1996;32:87–102.
[115] Bryk T, Mryglod I. Generalized hydrodynamics of binary liquids: transverse collective modes. Phys Rev E. 2000 Aug;62:2188–2199.
[116] Bryk T, Mryglod I. Concentration fluctuations and boson peak in a binary metallic glass: A generalized collective modes study. Phys Rev B. 2010 Nov;82:174205.
[117] Del Rio BG, Pascual P, Rodriguez R, et al. First principles determination of some static and dynamic properties of the liquid 3d transition metals near melting. Condens Matter Phys. 2020;23:23606.
[118] Del Rio BG, Gonzalez LE. Longitudinal, transverse, and single-particle dynamics in liquid Zn: ab initio study and theoretical analysis. Phys Rev B. 2017 Jun;95:224201.
[119] Del Rio BG, Gonzalez LE, Gonzalez DJ. Ab initio study of several static and dynamic properties of bulk liquid Ni near melting. J Chem Phys. 2017 Jan;146:034501.
[120] Guarini E, De Francesco A, Bafile U, et al. Neutron Brillouin scattering and ab initio simulation study of the collective dynamics of liquid silver. Phys Rev B. 2020 Aug;102:054210.
[121] Hosokawa S, Inui M, Matsuda K, et al. Damping of the collective modes in liquid Fe. Phys Rev B. 2008 May;77:174203.

[122] Bafile U, Guarini E, Barocchi F. Collective acoustic modes as renormalized damped oscillators: unifled description of neutron and x-ray scattering data from classical fluids. Phys Rev E. 2006 Jun;73:061203.
[123] Bryk T. Non-hydrodynamic collective modes in liquid metals and alloys. Eur Phys J Special Topics. 2011 May;196:65–83.
[124] D'Angelo G, Conti Nibali V, Wanderlingh U, et al. Multiple interacting collective modes and phonon gap in phospholipid membranes. J Phys Chem Lett. 2018 Jul;9:4367–4372.
[125] Zanatta M, Fontana A, Orecchini A, et al. Inelastic neutron scattering investigation in glassy $SiSe_2$: complex dynamics at the atomic scale. J Phys Chem Lett. 2013 Mar;4:1143–1147.
[126] Inui M, Koura A, Kajihara Y, et al. Peculiar atomic dynamics in liquid GeTe with asymmetrical bonding: observation by inelastic x-ray scattering. Phys Rev B. 2018 May;97:174203.
[127] Verkerk P. Dynamics in liquids. J Phys Condens Matter. 2001 Aug;13:7775–7799.
[128] Ruocco G, Sette F, Bergmann U, et al. Equivalence of the sound velocity in water and ice at mesoscopic wavelengths. Nature. 1996 Feb;379:521–523.
[129] Burns CA, Platzman PM, Sinn H, et al. Evidence for an instability near twice the fermi wave vector in the low electronic density liquid metal Li $(NH_3)_4$. Phys Rev Lett. 2001 Mar;86:2357–2360.
[130] Maradudin AA, Ambegaokar V. Calculation of the scattering function S (k, ω)for the inelastic scattering of neutrons by anharmonic crystals. Phys Rev. 1964 Aug;135: A1071–A1080.
[131] Pathak KN. Theory of Anharmonic Crystals. Phys Rev. 1965 Aug;139:A1569–A1580.
[132] Blairs S. Correlation between surface tension, density, and sound velocity of liquid metals. J Colloid and Interface Science. 2006 Oct;302:312–314.
[133] Khrapak SA. Practical dispersion relations for strongly coupled plasma fluids. AIP Adv. 2017 Dec;7:125026.
[134] Kryuchkov NP, Brazhkin VV, Yurchenko SO. Anticrossing of longitudinal and transverse modes in simple fluids. J Phys Chem Lett. 2019 Jul;10:4470–4475.
[135] Khrapak SA, Khrapak AG, Kryuchkov NP, et al. Onset of transverse (shear) waves in strongly-coupled Yukawa fluids. J Chem Phys. 2019 Mar;150:104503.
[136] Bryk T, Gorelli FA, Mryglod I, et al. Behavior of Supercritical Fluids across the "Frenkel Line". J Phys Chem Lett. 2017 Sep;8:4995–5001.
[137] Brazhkin VV, Prescher C, Fomin YD, et al. Comment on "Behavior of supercritical fluids across the 'Frenkel Line. J Phys Chem B. 2018 May;122:6124–6128.
[138] Bryk T, Gorelli FA, Mryglod I, et al. Reply to "Comment on 'behavior of supercritical fluids across the Frenkel Line. J Phys Chem B. 2018 May;122:6120–6123. Reply to. .
[139] Mokshin AV, Khusnutdinov RM, Akhmerova AR, et al. Universality of microscopic structural and dynamic features in liquid alkali metals near the melting point. JETP Lett. 2017 Sep;106:366–370.
[140] Giordano VM, Monaco G. Universal acoustic dispersion in liquid alkali metals. Phys Rev B. 2009 Jan;79:020201(R).
[141] Shaw GH, Caldwell DA. Sound-wave velocities in liquid alkali metals studied at temperatures up to 150°C and pressures up to 0.7 GPa. Phys Rev B. 1985 Dec;32:7937–7947.
[142] Scopigno T, Balucani U, Ruocco G, et al. Evidence of two viscous relaxation processes in the collective dynamics of liquid lithium. Phys Rev Lett. 2000 Nov;85:4076–4079.

[143] Scopigno T, Balucani U, Ruocco G, et al. Inelastic x-ray scattering study of the collective dynamics in liquid sodium. Phys Rev E. 2002 Mar;65:031205.
[144] Monaco A, Scopigno T, Benassi P, et al. Collective dynamics in molten potassium: an inelastic x-ray scattering study. J Chem Phys. 2004 Apr;120:8089–8094.
[145] Bodensteiner T, Morkel C, Glaser W, et al. Collective dynamics in liquid cesium near the melting point. Phys Rev A. 1992 Apr;45:5709–5720.
[146] Pilgrim W-C, Hosokawa S, Saggau H, et al. Temperature dependence of collective modes in liquid sodium. J Non-Crystalline Solids. 1999 Aug;250-252:96–101.
[147] Demmel F, Pasqualini D, Morkel C. Inelastic collective dynamics of liquid rubidium with increasing temperature by neutron scattering studies. Phys Rev B. 2006 Nov;74:184207.
[148] Kittel C. Quantum Theory of Solids. New York (NY): John Wiley & Sons, Inc; 1987.
[149] Baus M, Hansen J-P. Statistical mechanics of simple coulomb systems. Phys Rep. 1980 Mar;59:1–94.
[150] Bohm D, Staver T. Application of collective treatment of electron and ion vibrations to theories of conductivity and superconductivity. Phys Rev. 1951 Nov;84:836–837.
[151] Giustino F. Electron-phonon interactions from first principles. Rev Modern Phys. 2017 Feb; 89: 015003. Erratum Rev. Mod. Phys. 2019 Jan; 91: 019901.
[152] Baroni S, de Gironcoli S, Dal Corso A, et al. Phonons and related crystal properties from density-functional perturbation theory. Rev Modern Phys. 2001 Jul;73:515–562.
[153] Fasolato C, Sacchetti F, Postorino P, et al. Ultrafast plasmon dynamics in crystalline LiF triggered by intense extreme UV pulses. Phys Rev Lett. 2020 May;124:184801.
[154] Zubarev DN. Double-Time green functions in statistical physics. Sov Phys Usp. 1960 Nov-Dec;3:320–345.
[155] Paciaroni A, Comez L, Longo M, et al. Terahertz collective dynamics of DNA as affected by hydration and counterions. J Mol Liq. 2020 Nov;318:113956.
[156] Blairs S. Correlation between surface tension, density, and sound velocity of liquid metals. J Colloid Interface Sci. 2006 Oct;302:312–314.
[157] Zhang Y, Evans JRG, Yang S. Corrected values for boiling points and enthalpies of vaporization of elements in handbooks. J Chem Eng Data. 2011 Jan;56:328–337.
[158] Haynes WM editor, CRC Handbook of Chemistry and Physics (92nd ed.) Hoboken (NJ): CRC Press 4121–4123 (2011), ISBN 143955110.
[159] Bove LE, Sacchetti F, Petrillo C, et al. Neutron Investigation of the ion dynamics in liquid mercury: evidence for collective excitations. Phys Rev Lett. 2001 Nov;87:215504.
[160] Hosokawa S, Sinn H, Hensel F, et al. Short-wavelength collective excitations in liquid mercury investigated by inelastic X-ray scattering. Appl Phys A. 2002;74:S1648–S1650. [[Suppl.]].
[161] Bove LE, Sacchetti F, Petrillo C, et al. Dynamic structure factor of liquid mercury. J Non-Crystalline Solids. 2002 Sep;307-310:842–847.
[162] Bove LE, Sacchetti F, Petrillo C, et al. Self-dynamics and collective dynamics of liquid mercury. Philos Mag B. 2002;82:365–374.
[163] Badyal YS, Bafile U, Miyazaki K, et al. Cage diffusion in liquid mercury. Phys Rev E. 2003 Dec;68:061208.
[164] Calderín L, González LE, González DJ. Ab initio molecular dynamics study of the static, dynamic, and electronic properties of liquid mercury at room temperature. J Chem Phys. 2009 May;130:194502.
[165] Patty M, Schoen K, Montfrooij W. Fluctuating magnetic moments in liquid metals. Phys Rev E. 2006 Feb;73:021202.
[166] Meyer RE. Self-diffusion of liquid mercury. J Phys Chem. 1961 Mar;65:567–568.

[167] Nachtrieb NH, Petit J. Self-Diffusion in Liquid Mercury. J Chem Phys. 1956;24:746–750.
[168] Kamitakahara WA, Smith HG. Lattice-dynamics and electron-phonon interaction in solid mercury. Bull Am Phys Soc. 1975; 20: 299–1299. (Meeting Abstract).
[169] Ishikawa D, Inui M, Matsuda K, et al. Fast sound in expanded fluid Hg accompanying the metal-nonmetal transition. Phys Rev Lett. 2004 Aug;93:097801.
[170] Inui M, Ishikawa D, Matsuda K, et al. Observation of fast sound in metal–nonmetal transition in liquid Hg. J Phys Chem Solids. 2005 Dec;66:2223–2229.
[171] Young DA. Phase diagrams of the elements. Berkeley, Los Angeles, Oxford: University of California Press; 1991. (ISBN 0–520-07483–1).
[172] Bermejo FJ, García-Hernández M, Martinez JL, et al. Microscopic Dynamics of Liquid Gallium. Phys Rev E. 1994 Apr;49:3133–3142.
[173] Bermejo FJ, Fernández-Perea R, Alvarez M, et al. Collective, short-wavelength excitations in liquid gallium. Phys Rev E. 1997 Sep;56:3358–3369.
[174] Bove LE, Formisano F, Sacchetti F, et al. Vibrational dynamics of liquid gallium at 320 and 970K. Phys Rev B. 2005 Jan;71:014207.
[175] Scopigno T, Filipponi A, Krisch M, et al. High-Frequency acoustic modes in liquid gallium at the melting point. Phys Rev Lett. 2002 Dec;89:255506.
[176] Hosokawa S, Pilgrim W-C, Sinn H, et al. Microscopic dynamics in trivalent liquid Ga. Physica B. 2004 Jul;350:262–264.
[177] Inui M, Takeda S, Uechi TJ. Ultrasonic velocity and density measurement of liquid Bi–Ga alloys with miscibility gap region. J Phys Soc Jpn. 1992;61:3203–3208.
[178] Khusnutdinoff RM, Cockrell C, Dicks OA, et al. Collective modes and gapped momentum states in liquid Ga: experiment, theory, and simulation. Phys Rev B. 2020 Jun;101:214312.
[179] Demmel F. Slow structural relaxation process facilitates solidification in liquid gallium. Phys Rev B. 2020; Jan;101:014207.
[180] Yagodin DA, Filippov VV, Popel PS, et al. Density and ultrasound velocity in Ga-Bi melts. 13th International Conference on Liquid and Amorphous Metals. J Phys. 2008;98:062019.
[181] Buttersack T, Mason PE, McMullen RS, et al. Photoelectron spectra of alkali metal–ammonia microjets: from blue electrolyte to bronze metal. Science. 2020 Jun;368:1086–1091.
[182] Cohen MH, Thompson JC. The electronic and ionic structures of metal-ammonia solutions. Adv Phys. 1968;17:857–907.
[183] Thompson JC. Metal-nonmetal transition in metal-ammonia solutions. Rev Mod Phys. 1968 Oct;40:704–710.
[184] Heinzinger K. Computer simulations of metal-liquid ammonia solutions. J Mol Liq. 2000 Oct;88:77–85.
[185] Howard CA, Thompson H, Wasse JC, et al. Formation of giant solvation shells around fulleride anions in liquid Ammonia. J Am Chem Soc. 2004 Sep;126:13228–13229.
[186] Wasse JC, Hayama S, Skipper NT, et al. Structure of a metallic solution of lithium in ammonia. Phys Rev B. 2000 May;61:11993–11997.
[187] Zurek E, Edwards PP, Hoffmann R. A molecular perspective on lithium-ammonia solutions. Angew Chem Int Ed. 2009 Oct;48:8198–8232.
[188] Chuev GN, Quémerais P, Crain J. Nature of the metal–nonmetal transition in metal–ammonia solutions I. Solvated Electrons at Low Metal Concentrations. J. Chem. Phys. 2007 Dec;127:244501–244517.

[189] Chuev GN, Quémerais P. Nature of metal–nonmetal transition in metal–ammonia solutions II. From uniform metallic state to inhomogeneous electronic microstructure. J. Chem. Phys. 2008 Apr;128:144503–144512.
[190] Chaban VV, Prezhdo OV. Electron solvation in liquid ammonia: lithium, sodium, magnesium, and calcium as electron sources. J Phys Chem B. 2016 Feb;120:2500–2506.
[191] Chieux P, Sienko MJ, DeBaecker F. Neutron diffraction study and phase diagram investigation of the solid lithium-ammonia compound. J Phys Chem. 1975 Dec;79:2996–3000.
[192] Hayama S, Skipper NT, Wasse JC, et al. X-ray diffraction studies of solutions of lithium in ammonia: the structure of the metal–nonmetal transition. J Chem Phys. 2002 Feb;116:2991–2996.
[193] Thompson H, Wasse JC, Skipper NT, et al. Structural studies of ammonia and metallic lithium–ammonia solutions. J Am Chem Soc. 2003 Feb;125:2572–2581.
[194] Wasse JC, Hayama S, Masmanidis S, et al. The structure of lithium–ammonia and sodium–ammonia solutions by neutron diffraction. J Chem Phys. 2003 Apr;118:7486–7494.
[195] Burns C, Giura P, Said A, et al. Electronic Interactions in the expanded metal compound Li–$NH_3$. Phys Rev Lett. 2002 Nov;89:236404.
[196] Said AH, Burns CA, Alp EE, et al. Collective excitations in metal-ammonia systems as a function of electron density. Phys Rev B. 2003 Sep;68:104302.
[197] Giura P, Angelini R, Burns CA, et al. Electron correlation effects on the dielectric function of liquid metals. arXiv:cond-mat/. 2003 Oct;0310336:22.
[198] Sacchetti F, Guarini E, Petrillo C, et al. Giant electron-driven anomaly in the ion dynamics of a saturated solution of lithium in deuterated ammonia, Phys. Phys Rev B. 2003 Jan;67:014207.
[199] Petrillo C, Sacchetti F, Guarini E, et al. Collective modes in a saturated lithium-ammonia solution as a probe of the response of the low-density homogeneous electron gas. Phys Rev B. 2011 Sep;84:094206.
[200] Petrillo C, Sacchetti F, Guarini E, et al. The unpublished data are from an experiment performed at IN8 spectrometer, ILL, and are discussed in a forthcoming publication.
[201] Bowen DE, Thompson JC, Millett WE. Velocity of ultrasound in lithium-ammonia solutions. Phys Rev. 1968 Apr;168:114–120.
[202] Zhang X, Ai J, Ma Z, et al. Liquid metal based stretchable magnetoelectric films and their capacity for mechanoelectrical conversion. Adv Func Mater. 2020;30:2003680.
[203] Yu Z, Chen Y, Yun FF, et al. Discovery of a voltage-stimulated heartbeat effect in droplets of liquid gallium. Phys Rev Lett. 2018 Jul;121:024302.
[204] Sun X, Cui B, Yuan B, et al. Liquid metal microparticles phase change medicated mechanical destruction for enhanced tumor Cryoablation and dual-mode imaging. Adv Func Mater. 2020;30:2003359.
[205] Wallace DC. Liquid dynamics theory of high-temperature specific heat. Phys Rev E. 1998 Feb;57:1717–1722.
[206] Russell RA, Garvey CJ, Darwish TA, et al. Chapter five - biopolymer deuteration for neutron scattering and other isotope-sensitive techniques.In Methods in Enzymology. 2015; Vol. 565: 97–121. https://www.ill.eu/users/support-labs-infrastructure/deuteration-laboratory
[207] Paciaroni A, Orecchini A, Haertlein M, et al. Vibrational collective dynamics of dry proteins in the terahertz region. J Phys Chem B. 2012 Feb;116:3861–3865.